EVALUATING THE CO-ENCAPSULATION OF DOXORUBICIN AND L-ASPARAGINASE IN PLL-G-PEG CO-POLYMER NANOPARTICLES

A thesis presented to the faculty of the Graduate School of Western Carolina University in partial fulfillment of the requirements for the degree of Masters of Science in Chemistry.

By

Riley J. Hatton

Advisor: Dr. Rangika Hikkaduwa Koralege
Associate Professor of Chemistry
Department of Chemistry & Physics

Committee Members: Dr. Channa De Silva, Chemistry & Physics
Dr. Heather Coan, Biology
Dr. Curtis Beimborn, Chemistry & Physics

April 2025

ACKNOWLEDGEMENTS

I dedicate this thesis to my research advisor, Dr. Rangika Hikkaduwa Koralege, whose guidance and mentorship have been instrumental throughout my time at Western Carolina University. Dr. K has not only expanded my knowledge as a student but also strengthened my foundation as a scientist. Her persistence and unwavering support have been key to my success in research. She has instilled in me values that I will carry throughout my career and life, applying them to every challenge and accomplishment. Thank you for being an exceptional mentor.

I am also deeply grateful to my committee members, Dr. Channa De Silva, Dr. Heather Coan, and Dr. Curtis Beimborn, for their invaluable feedback and guidance throughout this project. Their expertise and insight provided the necessary support to ensure its success. I would also like to thank fellow chemist Dallas Dean for her consistent support and willingness to lend a hand whenever needed. Additionally, I would like to express my appreciation to Mr. Wes Bintz for his coordination in securing chemicals and supplies and to Mr. Matt Burleson for his instrumental training and technical assistance—this project would not have been completed without their help.

I extend my heartfelt thanks to my parents, family, and friends for their unwavering support and patience throughout my academic journey at Western. Their constant encouragement has been a pillar of strength, guiding me through every challenge. I am especially grateful to my grandmothers for their generosity and for instilling in me a strong work ethic—an invaluable gift that has motivated me to persevere and complete this project. My family has shaped me into the person I am today, and for that, I am forever thankful.

Finally, I would like to express my appreciation to Western Carolina University and the many faculty and staff members who have influenced my academic experience. I am especially thankful to God for granting me the opportunity to study at WCU, for which I will always be grateful. My time at Western has been a true blessing, leaving a profound impact on me that I will carry forward every day.

TABLE OF CONTENTS

LIST OF TABLES

LIST OF FIGURES

LIST OF ABBREVIATIONS

ALL - Acute Lymphoblastic Leukemia
ATR-FTIR – Attenuated total reflectance Fourier transform infrared
ASN - Asparagine
ASNS - Asparagine Synthetase
BSA – Bovine Serum Albumin
DLS – Dynamic Light Scattering
DMSO - Dimethyl Sulfoxide
d.nm – Diameter in nanometers
DOX - Doxorubicin
DTSSP - 3,3’-dithiobis(sulfosuccinimidyl propionate)
Glu. - Glutaraldehyde
GSH - Glutathione
^{1}H NMR - Proton Nuclear Magnetic Resonance
HPLC - High-Performance Liquid Chromatography
L-ASNase - L-asparaginase
PALS - Phase Analysis Light Scattering
PBS – Phosphate buffered saline
PDI – Polydispersity index
PEG – Poly(ethylene glycol)
PLL – Poly-L-lysine
PLL-g-PEG – Poly-L-lysine-grafted-poly(ethylene) glycol
MAL-PEG-NHS - Heterobifunctional maleimide-PEG-succinimidyl carboxymethyl NHS ester
mPEG-NHS – Methoxy poly-ethylene glycol N-hydroxysuccinimide
NPs – Nanoparticles
SDS-PAGE - Sodium Dodecyl Sulfate Polyacrylamide Gel Electrophoresis
SDDS - Smart Drug Delivery System
STEM – Scanning transmission electron microscope
UV-Vis - Ultraviolet-Visible

ABSTRACT

Cancer is a leading cause of death worldwide, with more than 10 million deaths reported in 2020. Leukemia is a type of blood cancer that can be difficult to treat in adults, requiring the development of Smart Drug Delivery Systems (SDDS). SDDS employ the use of nanoparticles (NPs) for targeted drug delivery. NPs are typically defined as falling in the size range of 1 – 1,000 nanometers. Nanotechnology has profound applications, specifically in the field of drug delivery. This includes nanocarriers as delivery vehicles, including polymeric NPs, quantum dots, liposomes, micelles, and many others. Polymeric NPs are synthesized using polymers. For instance, poly-L-lysine (PLL), a cationic polymer, is regularly employed to foster self-assembly in NPs formation. poly(ethylene glycol) (PEG) can be grafted to PLL to offer protection from proteolytic degradation. L-asparaginase (L-ASNase) is a therapeutic protein used to treat leukemia. Its mechanism involves converting asparagine (L-ASN) into aspartic acid, thereby depleting circulating asparagine a vital nutrient for cellular growth and protein synthesis. Leukemia cells are unable to produce asparagine and require an exogenous source and hence L-ASNase triggers asparagine starvation and cell death of leukemic cells. However, L-ASNase is hindered by a short circulatory half-life, diminished enzymatic activity under physiological conditions, and overall low stability. Previous research has demonstrated the encapsulation of L-ASNase in poly-l-lysine grafted poly(ethylene glycol) (PLL-g-PEG) nanocarriers to mitigate these drawbacks. Doxorubicin (DOX) is a small-molecule chemotherapeutic drug that is a topoisomerase II inhibitor. Topoisomerase II is necessary for transcription and DNA replication by repairing damaged or tangled DNA. DOX prevents topoisomerase II from repairing DNA, causing cell death. Co-encapsulation has emerged as a promising area of research. Co-encapsulation is the combining of multiple therapeutics into one nanocarrier. This presents unique challenges due to the different physicochemical characteristics of therapeutic molecules.

This research investigates the co-encapsulation of DOX and L-ASNase within a PLL-g-PEG polymer nanocarrier. The main goal of this research is to evaluate the co-encapsulation of DOX and L-ASNase within PLL-g-PEG NPs. Three different types of NPs have been synthesized: L-ASNase NPs, L-ASNase/DOX NPs, and L-ASNase/BSA-DOX NPs. These sets were synthesized to compare and evaluate two different methods of co-encpasulation. The specific tasks of this research were to (1) synthesis and characterization of L-ASNase and DOX encapsulated PLL-g-PEG NPs, (2) conjugation of DOX to Bovine Serum Albumin (BSA) through DTSSP linker and characterization using attenuated total reflectance Fourier transform infrared (ATR-FTIR) and ultraviolet-visible (UV-Vis) spectroscopy, (3) evaluation of NPs size, surface charge, and morphology through dynamic light scattering (DLS) and scanning transmission electron microscopy (STEM), (4) evaluation of the extent of protein/drug encapsulation (encapsulation efficiency) and stability using gel electrophoresis and DOX calibration curves, and (5) determination of L-ASNase activity within NPs.

In this study, we successfully synthesized co-encapsulated DOX and L-ASNase PLL-g-PEG polymer NPs. DOX was conjugated to the surface of BSA through a reducible linker to stabilize DOX within the NPs. The NPs were formed through self-assembly caused by electrostatic interactions between cationic co-polymer and negatively charged conjugates and proteins. L-ASNase/BSA-DOX NPs demonstrated lower size variability and smaller hydrodynamic diameters, averaging around 84.8 ± 48.0 nm. L-ASNase activity was not conversely affected more than typically observed from encapsulation of L-ASNase. BSA-DOX conjugates showed a higher affinity for NPs formation over L-ASNase, resulting in decreased L-ASNase encapsulation efficiencies ranging from 75 – 94%. DOX remains stably encapsulated within L-ASNase/BSA-DOX NPs, producing high DOX encapsulation efficiencies. This method of co-encapsulation serves as a model for the co-encapsulation of other proteins and small molecule drugs.

CHAPTER I

INTRODUCTION

1.1—Leukemic Cancers and Protein Therapy

Cancer is a predominant cause of death worldwide, accounting for nearly 10 million deaths in 2020 [1]. Leukemia is a specific type of cancer that primarily targets white blood cells. This type of cancer originates in the bone marrow, where white blood cell production occurs. White blood cells are a critical regulator of the immune system. Leukemia has two primary risks: immunosuppression and overcrowding of healthy hematopoietic cells [2]. Leukemia cases typically originate in two types of blood stem cells: myeloid and lymphocytic stem cells [2]. Myeloid stem cells produce red blood cells, platelets, and different white blood cells, such as neutrophils. Lymphocytic stem cells produce only white blood cells, such as B-cells and T-cells [3]. Leukemia can be classified as either acute or chronic [4]. Acute leukemia is characterized by rapid cellular division and quick progression. These cells are unable to function like normal lymphocytes. Chronic leukemia is mildly aggressive and is characterized by slow cellular division [4]. The lymphoblasts produced in chronic leukemia retain the partial functionality of normal lymphocytes, making detection much more difficult [5].

Widely used conventional therapies for cancer treatment include chemotherapy, radiotherapy, surgery, and local therapies, such as focused ultrasound and specific drugs targeting [6]. As a result of toxic side effects, low specificity, and resistance to the treatment present in most conventional cancer therapies, SDDS have emerged as a promising strategy for targeted cancer therapy. In SDDS, advanced methods are used to deliver active drug molecules to selectively accumulate in the diseased tissue for a prolonged time. These methods utilize highly controllable drug release mechanisms to enhance their therapeutic effects and to reduce related side effects. Furthermore, these drug delivery systems allow for the simultaneous delivery of drugs and/or therapeutic proteins (co-delivery), allowing for synergistic effects and enhanced anti-tumor activity. Therefore, SDDS have received a greater preference over conventional anticancer therapies in recent years. Different types of smart drug delivery vehicles, generally referred to as nanocarriers, have been developed [6][7].

L-ASNase is widely used as a therapeutic protein for the treatment of hematopoietic diseases such as acute lymphoblastic leukemia (ALL) and lymphomas since 1970 [8][9]. The antitumor activity of L-ASNase relies on the fact that cancerous lymphoblasts cannot synthesize sufficient levels of (ASN) due to the down-regulation of asparagine synthetase (ASNS) in their cells. Therefore, compared to normal cells, ASN becomes an essential amino acid for malignant cells for their survival. A supply of large amounts of ASN is indeed necessary for ALL cell growth, and this is solely dependent on the availability of extracellular ASN in the bloodstream. Depletion of circulating ASN by intravenous or intramuscular administration of L-ASNase results in starvation and selective apoptosis of the leukemic cells. It has been reported that reducing the concentration of L-ASNase in circulating blood from 50 to ≤ 3 μM during treatment with L-ASNase prevents leukemia cells from continuing the cell cycle. Despite its prime use in the treatment of ALL, L-ASNase has shown therapeutic potential for use in other types of cancer, including acute myeloid leukemia, ovarian cancer, brain cancer, prostate cancer, pulmonary adenocarcinoma, non-Hodgkin lymphoma, chronic lymphoid leukemia and sarcomas such as lymphosarcoma, reticulosarcoma and melanosarcoma [10][11][12][13][14][15].

1.2—Nanoparticles and Applications of Nanotechnology in Drug Delivery

Nanoscience is an interdisciplinary field that investigates nano-scale materials to identify and utilize their diverse physicochemical properties in various applications [16]. The nano-scale is defined as in the range of 1 – 1,000 nanometers (nm) [17]. Nanomaterials and NPs exhibit broad applications across numerous industries, including engineering, healthcare, and drug delivery. Nano-scale materials often show properties not observed in the same macro-scale or bulk materials. For example, specific inorganic nanomaterials demonstrate magnetic or electrical properties distinctive from their bulk counterparts. These properties are predominantly attributed to the increased surface area-to-volume ratio [18]. The physicochemical differences between nanomaterials and bulk materials offer distinct advantages. The advantages of NPs are already being exploited in numerous industries, such as cosmetics and sunscreen [19]. Another area of promise is in the field of drug delivery. A consistent challenge observed in treatments for various diseases is the effective delivery of high drug or therapeutic concentrations. NPs can facilitate a pathway to increase efficient drug delivery. [20] Many diverse types of NPs are used in drug delivery research, including micelles, liposomes, quantum dots, polymeric, and many others [20]. Depending on the nanomaterial used, drugs and therapeutics can be delivered in two ways: surface-adsorbed or encapsulated [21]. Drug delivery-based NPs are synthesized primarily using two approaches. These approaches are a top-down method, where the starting materials are in bulk and broken into fragments, and a bottom-up approach, where small portions of nanomaterials are combined to form NPs [22].

1.3—Polymeric NPs Used in Drug Delivery

Polymeric NPs are a subset of NPs synthesized using polymers. NPs can be synthesized using a wide array of polymers. Frequently used polymers in NPs synthesis are poly(lactic-co-glycolic acid) (PLGA), dextran, PEG, polyvinyl alcohol (PVA), and PLL [23]. The distinct physicochemical properties associated with each polymer offer unique applications and functionality. Hydrophobic and hydrophilic polymer reactions form NPs stabilized through interactions with changing solvents [24]. Some polymers have overall positive or negative charges. PLL is a cationic polymer that carries a positive charge due to its protonated primary amine groups at physiological pH, allowing it to interact with negatively charged molecules. PEG and many other polymers like PLGA can offer increased protection from proteolytic degradation [25]. Many of these attributes can be combined through the synthesis of co-polymers.

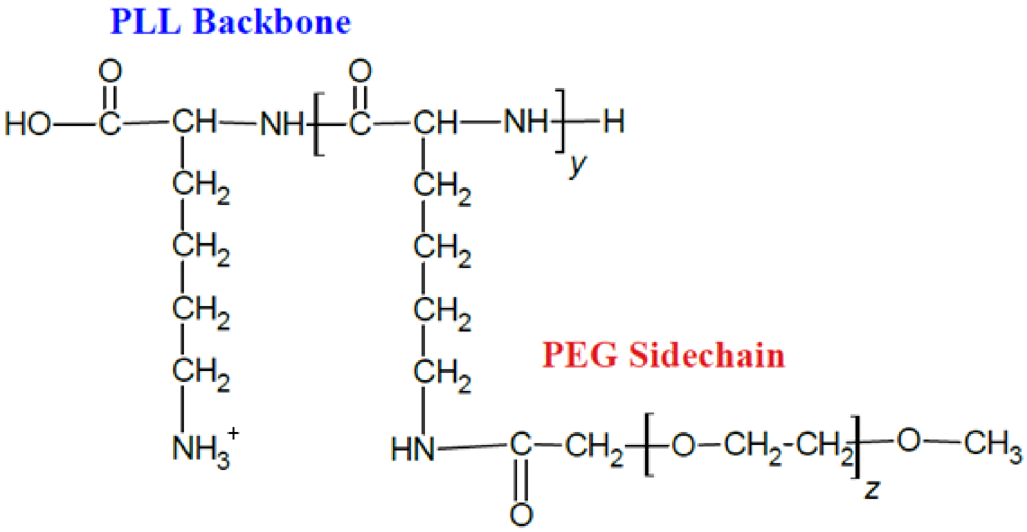

Figure 1. Chemical structure of PLL-g-PEG Co-polymer.

For instance, PLL-g-PEG is a co-polymer synthesized by grafting several PEG moieties to one PLL chain [25]. This co-polymer has the paired benefits of an increased affinity for negatively charged molecules and enhanced protection from proteolytic degradation. Polymeric NPs are usually synthesized through self-assembly methods, primarily electrostatic and hydrophobic/hydrophilic interactions [26][27]. Due to the physicochemical properties associated with each polymer, polymeric NPs can have crucial advantages over other types of NPs. Once synthesized, polymeric NPs often demonstrate strong stability. Another impressive advantage is that drugs and therapeutics can be released in a controlled and stimuli-responsive manner by exploiting certain physicochemical properties, such as pH or hydrolysis. Despite these advantages, there are a few drawbacks observed with polymer-based drug delivery. A major limitation is the difficulty of scaling up synthesis methods to produce large quantities of functional NPs [28]. However, the considerable benefits of polymeric NPs and their applications to drug delivery outweigh the limitations.

1.4—Therapeutic Proteins in Cancer Treatments

A significant number of cancer therapies utilize therapeutic protein drugs. These proteins are an emerging class of cancer therapeutics that presents distinct advantages, such as higher specificity and potency than small molecule drugs. However, protein drugs are vulnerable to environmental changes and immune responses, impairing their delivery to targeted tissues and organs [29]. Host immune systems regularly recognize bacterial proteins due to their origin and remove them from the host. The immunogenicity of therapeutic proteins limits their clinical efficacy and creates adverse life-threatening effects in patients. Therefore, protein therapies have been limited to minimally immunogenic proteins [29].

Therapeutic proteins can be broadly applied to various cancers. Protein p53, a well-known cancer-suppressing therapeutic protein, in the presence of another bacterial protein azurin, amplifies its tumor-suppressing activity by increasing apoptosis and autophagy [30]. Many therapeutic proteins are regularly utilized, such as MPT63 from Mycobacterium bovis, arginine deiminase from Mycoplasma arginine, and many different antibodies [31].

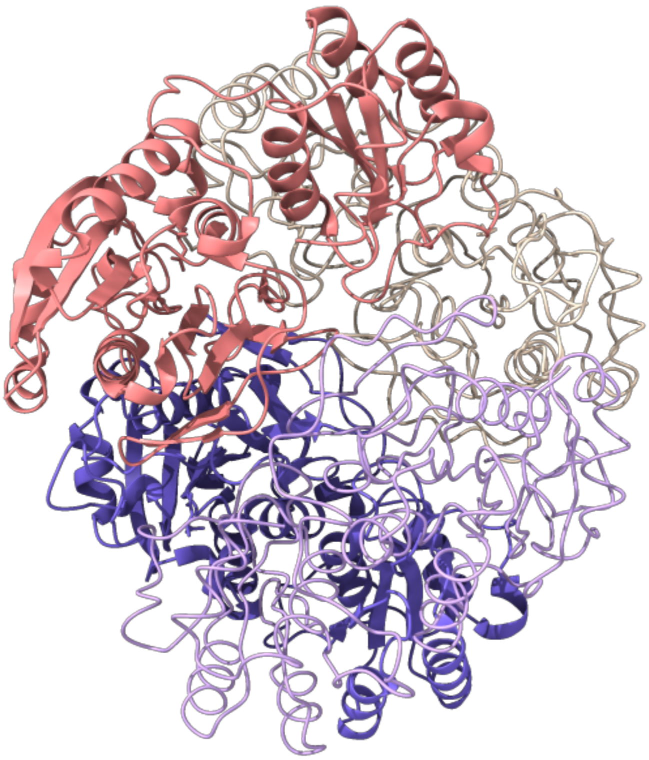

Figure 2. Protein structure of L-ASNase.

L-ASNase is another prominent therapeutic protein. This bacterial protein is specifically used in the treatment of acute lymphoblastic leukemia (ALL). Its protein structure is illustrated in Figure 2 [31]. This protein was first identified in 1904 and has become widely used for cancer treatment [32][33]. This protein is considered to have high efficacy in treating ALL as it significantly reduces cancer cell production and quickly induces cell apoptosis [33]. This enzyme is a tetramer at a molecular weight of 140 kDa that has been extensively characterized using both X-ray crystallography and small-angle X-ray scattering (SAXS) [34][35]. L-ASNase exhibits an isoelectric point ranging from 4.6 – 5.5, causing a net negative charge at neutral and alkaline pH conditions [36]. The observed primary function of L-ASNase is the hydrolysis of L-ASN to aspartic acid. ALL cells are ASN-dependent and cannot produce L-ASN due to the silencing of the ASNS gene, requiring an exogenous source. L-ASNase targets this vulnerability by converting available L-ASN into an unusable form. This is very effective at initiating cell death, and it destroys ASN-dependent tumors by degrading circulating L-ASN [33][37][38]. This treatment is limited by the short circulating lifetime of L-ASNase at physiological conditions, low stability, and reduced enzymatic activity at physiological conditions. To address these drawbacks, ongoing research is focusing on protein surface modifications, combination therapy, and SDDS [39][40].

1.5—Small Molecule Drugs Used in Cancer Therapies

There are many different treatment options for ALL. Molecule drugs are commonly used to combat advanced forms of cancer. There are numerous different types of drugs regularly used. The majority of chemotherapeutic drugs currently in use fall into the following categories: small molecule inhibitors, peptide drugs, and monoclonal antibodies [41]. Small molecule inhibitors have always shown high promise in cancer treatment. These drug molecules bind to specific proteins, receptors, etc., that prevent certain cellular processes from occurring. This can include gene expressions, metabolic pathways, and cell signaling [41]. For example, there are inhibitors, such as imatinib, that specifically target the tyrosine kinase pathway and prevent the uncontrolled production of abnormal oncoproteins [42][43]. Another very effective type is topoisomerase II inhibitors. During DNA replication, DNA can easily get tangled. Topoisomerase II is an enzyme that works specifically with DNA. It recognizes specific sequences to create controlled breaks in the double-helix structure. It then disentangles the DNA and anneals it back together to reform the correct functional double-helix structure [44]. Topoisomerase II inhibitors work by targeting this pathway. The protein is able to bind to the DNA structure and create breaks in the helix, but the inhibitors prevent the protein from annealing the DNA structure [45]. There are many different inhibitors, including etoposide, belotecan, pixantrone, and DOX [44].

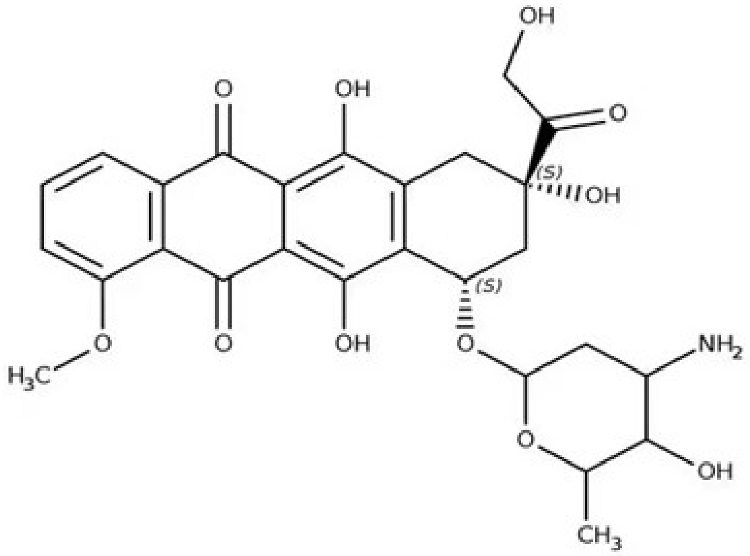

Figure 3. Chemical Structure of DOX.

DOX is a highly potent drug regarded as one of the most effective available chemotherapies. Its mode of action includes intercalation into DNA and inhibition of topoisomerase II, leading to changes in chromatin structure and generation of free radicals and oxidative damage to biomolecules [46]. It is an amphiphilic drug in the anthracycline antibiotic class. Its molecular structure is comprised of hydrophobic anthraquinone rings and a hydrophilic sugar group, allowing solubility in water and organic solvents. However, it is poorly soluble in salt or buffer solutions, forming a dimer in their presence [47]. The primary amine present in DOX allows for the formation of conjugates with other molecules and proteins using amine-reactive linkers without reducing cytotoxicity [48]. Conjugation enables the potential development of advanced drug delivery and optimization.

1.6—Co-delivery & Co-encapsulation

Co-delivery is an emerging treatment strategy for cancer. Co-delivery or combination therapy integrates multiple therapies to enhance treatment efficacy. Combining therapies and treatments allows for more targeted, specific cancer-based treatments. For example, combining drugs

5-fluorouracil (5-FU) and levofolinate shows increased efficacy in the treatment of pancreatic cancer [49]. Many potential synergistic combinations have yet to be thoroughly investigated or identified. Co-encapsulation has been proposed as a viable strategy to carry out co-delivery. This approach involves the simultaneous encapsulation of two therapeutics into a single nanocarrier. Numerous models of encapsulation have been adapted to this strategy. Liposomes serve as one of the most widely utilized nanocarriers for co-encapsulation. Daunorubicin and cytarabine are examples of this, having been successfully co-encapsulated within a liposomal nanocarrier [50]. Despite the potential advantages, co-encapsulation presents significant challenges. Due to drug compatibility, solubility, and physicochemical properties, combining therapies requires creatively identifying possible nanocarriers. Nanocarrier design can quickly increase in complexity, requiring multiple layers, modifications of polymers or biomolecules, and intricate synthesis methods to achieve co-encapsulation. Certain modifications can alter therapy functionality. For example, multilayered NPs can alter therapies' stability and physicochemical properties [50]. Following the successful development and optimization of a nanocarrier model, it can be applied to the co-encapsulation of other therapeutics, creating broad applicability.

1.7—Evaluation of the Co-encapsulation of DOX and L-ASNase in PLL-g-PEG Co-polymer NPs

This research aims to evaluate the co-encapsulation of a hydrophilic therapeutic protein, L-ASNase, and an amphiphilic small molecule cancer drug, DOX. The primary objective of this project is to achieve successful co-encapsulation of L-ASNase and DOX into a single nanocarrier. Previous research activities in our lab demonstrated the encapsulation of proteins within PLL-g-PEG co-polymers without affecting the proteins' therapeutic activity. As a cationic polymer, PLL allows for electrostatic interactions with negatively charged biomolecules, including proteins, therapeutics, or nucleic acids at physiological pH [51][52]. PEG provides protection from proteolytic degradation to the co-polymer when introduced into biological systems, prolonging the stability of nanocarrier complexes in the circulatory system [53]. L-ASNase is a charged protein with a net negative surface charge at physiological conditions.

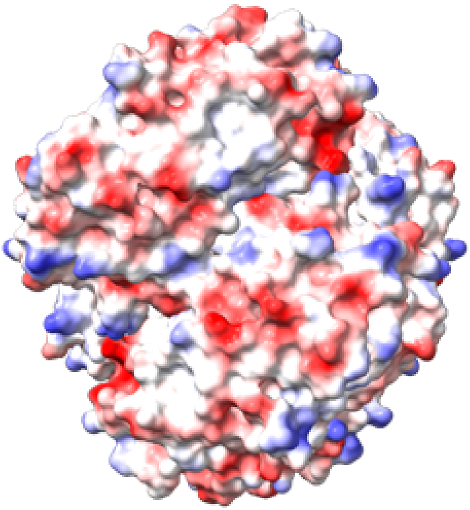

Figure 4. Surface charge map of L-ASNase. Red regions represent negative surface charges, and blue regions represent positive surface charges.

Using a previously developed method, co-encapsulation of L-ASNase and DOX within PLL-g-PEG polymeric NPs was carried out through electrostatic self-assembly, as depicted in Figure 5. DOX present in the surrounding solution is naturally co-encapsulated alongside L-ASNase.

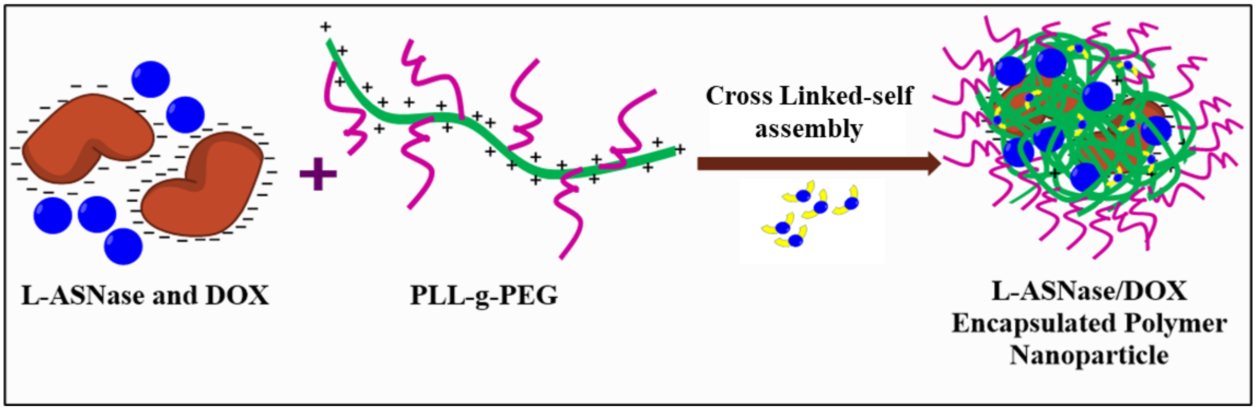

Figure 5 A schematic diagram of the self-assembly process of L-ASNase and DOX co-encapsulated NPs.

Integrating these therapies into a single delivery system could potentially enhance anti-tumor activity. Nanocarriers can be carried through the bloodstream, where red blood cells (RBCs) can provide prolonged therapeutic delivery due to their extended lifespan. Using RBCs as delivery vehicles has allowed for more effective drug targeting in blood-specific cancers [54][55]. Synthesized NPs are stabilized through crosslinking with glutaraldehyde (Glu.) or 3,3'-dithiobis(sulfosuccinimidyl propionate) (DTSSP). Glu., a non-reducible linker, stabilizes NPs for model/experimental applications. Crosslinking increases nanocarrier stability by preventing uncontrolled therapeutic release. Crosslinking occurs in free primary amines on the PLL-g-PEG co-polymer and the carbonyl groups of Glu. [56].

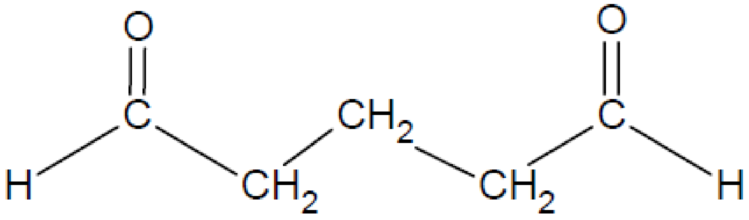

Figure 6 Chemical structure of Glu.

DTSSP is a non-toxic reducible crosslinker that functions similarly to Glu. The disulfide bond between the carbonyl groups in DTSSP is pH-reducible, allowing for the controlled release of the therapeutic drug from the NPs [57].

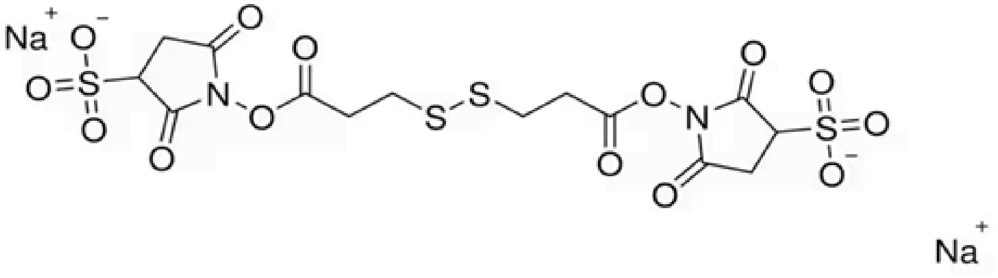

Figure 7 Chemical structure of DTSSP.

To prevent the uncontrolled release of DOX and enhance stability in buffered solutions, DOX was conjugated to BSA, forming BSA-DOX conjugates. BSA is a non-toxic model protein with a molecular weight of 66.5 kDa and net negative surface charge at physiological pH conditions, making it an effective candidate for PLL-g-PEG co-polymer encapsulation [58]. BSA possesses 30 – 35 surface lysine residues with primary amines available for conjugation to other molecules or proteins [59]. A surface charge map of BSA and a surface map of lysine residues on the BSA surface are shown in Figures 8 and 9, respectively.

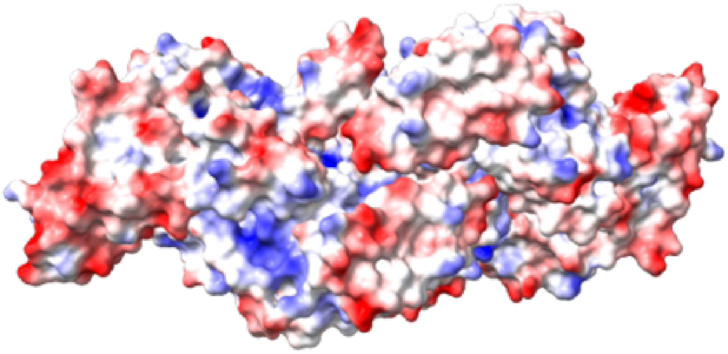

Figure 8 Surface charge map of BSA. Red regions represent negative surface charges, and blue regions represent positive surface charges.

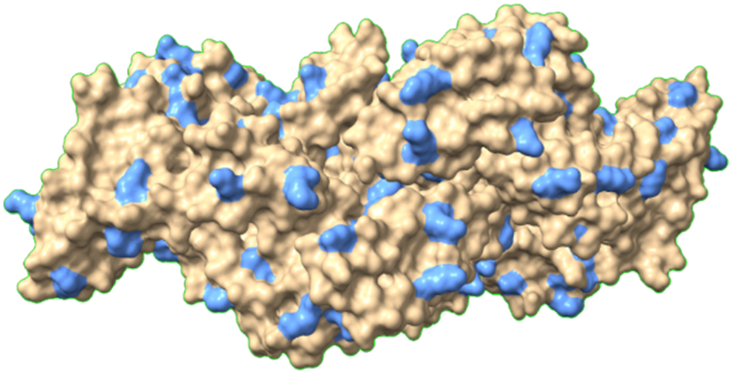

Figure 9 BSA surface map of lysine residues. Red regions represent negative surface charges, and blue regions represent positive surface charges.

As previously discussed, DOX contains a primary amine group with the potential for conjugation with other molecules [60][61]. This conjugation is achieved by utilizing DTSSP, a pH-reducible linker, allowing for controlled drug release and stabilization of DOX within the NPs, as shown in Figure 10.

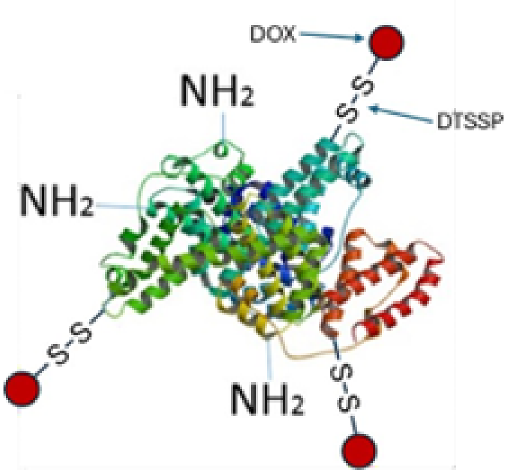

Figure 10 A schematic diagram of BSA showing free primary amine groups and some amine groups functionalized with DTSSP linker and DOX.

The co-encapsulation of BSA-DOX conjugates and L-ASNase followed the same electrostatic self-assembly method described above, and Figure 11 shows a schematic diagram of the self-assembly process.

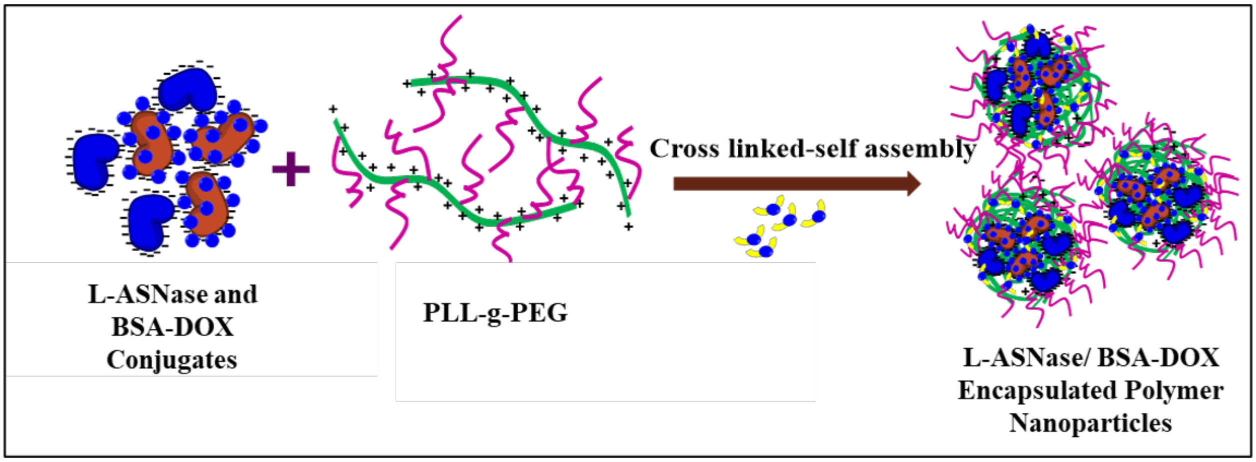

Figure 11 A schematic diagram of the self-assembly process of L-ASNase and BSA-DOX conjugates co-encapsulated NPs.

CHAPTER II

EXPERIMENTAL METHODS

2.1—Materials

PLL•HBr with a molecular weight of 15-30 kDa, L-ASNase, and asparaginase activity assay kit were purchased from Sigma-Aldrich. Heterobifunctional maleimide-PEG-succinimidyl carboxymethyl NHS ester (MAL-PEG-NHS) and methoxy poly-ethylene glycol N-hydroxysuccinimide (mPEG-NHS) with molecular weights of 5 and 2 kDa, respectively, were purchased from Creative PEGWorks. DOX HCl, DTSSP, BSA, Glu. (50%), acrylamide/bisacrylamide (37.5:1) and other polyacrylamide gel casting and running materials were purchased from Thermo Fisher Scientific. The reagents were used without further purification. Ultrapure water with a resistivity of 18.2MΩ was obtained from a Barnstead EASYpure II RF/UV Ultrapure Water System.

2.2—PLL-g-PEG Co-polymer Synthesis

The PLL-g-PEG co-polymer synthesis was carried out according to our previously published method [51][62]. To produce the co-polymer, the primary amine groups of the PLL backbone were modified with the succinimidyl ester group on the heterobifunctional PEG to produce PLL-g-PEG. To prepare PLL-g-PEG, 15 mg of 15-30 kDa PLL•HBr was dissolved in 200 µL of phosphate-buffered saline (PBS, pH 7.4), and a 50/50 mass ratio mixture of 2 kDa mPEG-NHS (20 mg) and 5 kDa MAL-PEG-NHS (20 mg) solids were added to the dissolved PLL. The mixture was allowed to react for 1 h before being washed three times with a 50/50 (v/v) mixture of PBS and ethanol and a final wash with pure ethanol in a 10 kDa centrifugal concentrator at 11,337 rcf. After the washing steps, the copolymer was air dried manually using an air valve before being used or stored at -20°C.

2.3—Proton Nuclear Magnetic Resonance Spectroscopy (^{1}H NMR) Analysis of PLL-g-PEG polymers

PLL-g-PEG copolymers (5 mg) were dissolved in 750 µL of deuterium oxide (D_2O) solvent and analyzed using Bruker 400 MHz NMR with a 5-mm tunable probe for ^{1}H NMR. This was done to confirm the grafting of PEG onto PLL using ^{1}H NMR spectroscopy.

$$\textit{Grafting Ratio} = \frac{\textit{Integration of -CH}_2\textit{CH}_2\textit{O- PEG Peak/ \# of H in -CH}_2\textit{CH}_2\textit{O- of PEG}}{\textit{Integration of -CH- PLL Peak/ \# of H in -CH- of PLL}} \qquad \textit{Equation 1}$$

2.4—ATR-FTIR Analysis of Co-polymer and BSA-DOX Conjugates

ATR-FTIR was performed on the PLL-g-PEG co-polymers, DOX, DTSSP, BSA, and BSA-DOX, to confirm their functionalities. A few milligrams of each sample were analyzed using a Thermo iS10 FT-IR Centarus Microscope with 128 scans performed at a resolution of 4 cm^{-1}.

2.5—NP Synthesis Methods

Three different types of NPs were synthesized: (1) L-ASNase NPs, (2) L-ASNase/DOX NPs, and (3) L-ASNase/BSA-DOX NPs. NPs were synthesized using the method described below. Modifications were made in the original procedure as needed for co-encapsulation of L-ASNase and DOX.

To synthesize L-ASNase NPs, a L-ASNase stock solution of 1 mg/mL was prepared by taking 0.500 (±0.001) mg of L-ASNase and dissolving in 0.50 mL of PBS. Samples of L-ASNase were encapsulated using PLL-g-PEG (15-30 kDa), with a co-polymer to protein mass ratio of 7:1. L-ASNase was dissolved in PBS to a concentration of 0.266 mg/mL and maleimide functionalized g-PEG copolymer was dissolved in PBS at a concentration of 6 mg/mL. The copolymer (7.5 µL) was then added to the L-ASNase solution (25 µL) dropwise while gently vortexing, followed by incubation of the mixture for 1 hour at room temperature. To stabilize the polyion complexes formed between the negatively charged L-ASNase and positively charged PLL-g-PEG, the free amino groups within the particles were cross-linked with 5 µL of Glu. solution (0.025% in PBS) or 5 µL of DTSSP (0.025% in PBS) and incubated for another 3 hours at room temperature.

To synthesize L-ASNase and DOX co-encapsulated NPs, the original synthesis method described above was slightly modified by combining 12.5 µL of 0.266 mg/mL L-ASNase and 12.5 µL of 0.266 mg/mL DOX before adding 7.5 µL of the 6 mg/mL co-polymer solution. To synthesize L-ASNase and BSA-DOX co-encapsulated NPs, DOX was conjugated to BSA using a disulfide linker, DTSSP, as described in section 3.5 below. The original NP synthesis method described above was slightly modified by combining 12.5 µL of 0.266 mg/mL L-ASNase and 12.5 µL of 0.266 mg/mL BSA-DOX before adding 7.5 µL of the 6 mg/mL co-polymer solution.

2.6—Chemical Conjugation of DOX to BSA using DTSSP Linker

A 1.0 mg/mL DOX solution was prepared by dissolving 1.000 (±0.001) mg of DOX in 1.00 mL of PBS (pH 8.4). This solution was centrifuged at 11,337 rcf for 5 minutes. The supernatant was poured off, and the remaining precipitate was dissolved in 1.00 mL of Dimethyl Sulfoxide (DMSO). 2.500 (±0.001) mg of BSA was dissolved in 1.00 mL of PBS (pH 6.0) to prepare a 2.5 mg/mL BSA solution. A 0.8 mg/mL DTSSP solution was prepared by dissolving 80.000 (±0.001) mg of DTSSP in 1.00 mL of PBS (pH 6.0). The chemical conjugation was carried out by combining 250 µL samples of DOX and BSA, followed by the dropwise addition of DTSSP (250 µL) while vortexing. To the resulting mixture, 0.3 L of triethylamine was added dropwise while vortexing. The solution was incubated for 30 minutes at room temperature, followed by washing 4 times in a 50 kDa centrifugal concentrator at 11,337 rcf for 5 minutes with 66:33 DMSO: PBS solution. The conjugated BSA-DOX was stored in the refrigerator at 4 °C overnight before use.

2.7—UV-Vis and FTIR Analysis of Conjugated BSA-DOX

UV-Visspectroscopic analysis was carried out on DOX, BSA, and BSA-DOX in an Agilent Cary 5000 UV-vis-NIR. The blank consisted of 66:33 PBS (pH 6): DMSO. Samples were run in triplicate.

Infrared Spectroscopy was performed on DOX, BSA, and BSA-DOX using a Thermo Nicolet iS10 FT-IR/Centarus Microscope with 128 scans performed at a resolution of 4.

2.8—Physicochemical Characterization of NPs

The size distribution of all NP samples (100 μL) was determined using DLS on a Malvern Zetasizer ZS Particle Size Analyzer equipped with a 4 mW 632.8 nm laser. All the measurements were done at 25 °C and using a Brand Tech Scientific ZEN0040 70 μL Ultra- Micro disposable cuvette with stopper. DLS experiments were run directly after synthesis.

The ζ-potential of NP samples was determined directly after synthesis using phase analysis light scattering (PALS) using a DTS1070 cell.

2.9—SDS-PAGE Gel Retardation Assay

The extent of L-ASNase and BSA-DOX encapsulation in NPs was determined by a gel retardation assay. Sodium dodecyl sulfate-polyacrylamide gel electrophoresis (SDS-PAGE) gels (12%) were hand cast and loaded with either NP samples or control of non-encapsulated L-ASNase and BSA proteins. NPs were run at 180 V under non-reducing conditions using a BIO-RAD Mini-PROTEAN® Tetra Cell apparatus until the dye front reached the bottom of the gel. The SDS-PAGE gels were stained with Coomassie G-250 before imaging using a gel imager.

2.10—STEM Analysis of NPs

The size and morphology of the NPs were analyzed using STEM. NP samples were diluted by 1500x with ultrapure water. NP samples (10 μL) was deposited onto Lacey/Formvar Carbon 200 mesh copper grids using a drop-casting method and allowed to air-dry at room temperature overnight. The sample was then negatively stained with 10 μL of 1% phosphotungstic acid (pH 7.4) for one minute, and the excess stain was wicked off the grid using filter paper. The samples were allowed to dry overnight before observation using a Thermo Fisher Apreo 2 SEM equipped with a TEM detector. A voltage of 30 kV and a current of 50 pA was used for analysis. Distribution profiles were developed using captured STEM images. The polydispersity index (PDI) was determined using Equation 2.

$$PDI = \left(\frac{St.\ Dev.}{Mean\ NPs\ Size}\right)^2 \qquad Equation\ 2$$

2.11—Determination of L-ASNase Activity of NPs

An asparaginase activity assay kit from Sigma-Aldrich was used to evaluate the activity of encapsulated L-ASNase in all types of NPs. Asparaginase activity was calculated by measuring the amount of aspartate generated in a coupled enzymatic reaction using colorimetric detection. A series of aspartate standard solutions were used as calibration standards. An aspartate standard solution of 1 mM was prepared using the 100 mM stock solution provided in the assay kit. Volumes of 0, 2, 4, 6, 8, and 10 μL of the 1 mM aspartate standard solution were added into a 96-well plate to generate 0 (blank), 2, 4, 6, 8, and 10 nmoles/well standards. An aliquot of asparaginase assay buffer was added to each well to bring the total volume of each well to 50 μL. A 50 μL aliquot of NP sample was used for the assay reaction. For the positive control, 5 μL of asparaginase assay positive control was used, and the final volume was adjusted to 50 μL with water. A total of 50 μL aliquot of assay reaction mix was added to each standard, sample, and positive control according to Table 1 below to bring the final volume of each well to 100 μL before analysis.

Table 1. Assay reaction mixes.

Reagent	Samples and Standards/μL	Sample Blank/μL
Asparaginase Assay Buffer	40	42
Substrate Mix	4	4
Aspartate Enzyme Mix	2	0
Conversion Mix	2	2
Fluorescent Peroxidase Substrate	2	2

The 96-well plate was then analyzed using a SpectraMax iD5 multimode plate reader at a wavelength of 570 nm.

2.12—Quantification of DOX in Co-encapsulated NPs

Seven DOX standards were prepared using serial dilution method ranging from 0-0.2 mg/mL and labeled A – G, with standard A and G being 0.20 and 0 mg/mL, respectively. Samples were washed to remove unencapsulated DOX in a 100 kDa centrifugal concentrator at 11,337 rcf. 100 µL of 10 mM of glutathione (GSH) was added to 200 µL of each sample. Samples were incubated 24 hrs at room temperature after GSH addition. A 100 µL sample of each DOX standard, L-ASNase NPs, and L-ASNase/DOX NPs were added in triplicate to a 96-well plate. A SpectraMax iD5 multimode microplate reader was used to record absorbance at 482 nm. A calibration curve prepared using the DOX standards was used to calculate the DOX concentration and amount (in mg) present in L-ASNase/DOX NPs. L-ASNase/BSA-DOX NPs were incubated in PBS (pH 3) for 24 hrs. to trigger the release of DOX from BSA-DOX conjugates before measuring the absorbance at 482 nm.

The DOX encapsulation efficiency was calculated using Equation 3, given below.

$$\textit{Encapsulation Efficiency} = \frac{\textit{Amount of DOX NPs (mg)}}{\textit{Total Amount of DOX added (mg)}} * 100 \qquad \textit{Equation 3}$$

2.13—High-Performance Liquid Chromatography (HPLC) Analysis

L-ASNase/DOX NPs and L-ASNase/BSA-DOX NPs were washed three times using 100 kDa centrifugal concentrators at 11,337 rcf, and the solvent was collected for analysis. A 0.0885 mg/mL DOX standard was prepared with PBS (pH 7.4) and DMSO. An isocratic HPLC method was utilized in the analysis of DOX present in solvent. The method was carried out using an Agilent Technologies 1220 Infinity LC equipped with a Merck C18 (4.6 mm x 100 mm) column and UV detector. A 1.0 mL/min flow rate was used, while UV detection was set at 233 nm. The mobile phase consisted of water:acetonitrile (30:70) and was adjusted to a pH of 3 using 85% phosphoric acid.

CHAPTER III

RESULTS AND DISCUSSION

This study aimed to co-encapsulate L-ASNase and DOX into a PLL-g-PEG co-polymer nanocarrier for efficient drug delivery. The co-encapsulation of a small molecule drug and a protein presents unique challenges due to different physicochemical characteristics, such as solubility and size. Previous research has demonstrated the successful encapsulation of L-ASNase in PLL-g-PEG co-polymers [52]. To the best of our knowledge, no prior studies have reported the encapsulation of DOX in PLL-g-PEG polymeric NPs.

Our initial hypothesis proposed that free DOX in the surrounding solution would co-encapsulate alongside L-ASNase during the self-assembly of NPs with the PLL-g-PEG co-polymer. However, due to its small size and the NP matrix, DOX undergoes premature and uncontrolled release from NPs into the surrounding solution as supported by our HPLC analysis. To avoid premature and uncontrolled release, we modified our approach to conjugate DOX on a protein before encapsulation. In our previous studies, BSA has served as a model protein to develop self-assembled NPs using PLL-g-PEG. Therefore, the conjugation of DOX on BSA has been utilized to stabilize DOX inside NPs and mitigate uncontrolled release. These BSA-DOX conjugates were then co-encapsulated along with L-ASNase. Thus, BSA-DOX conjugates and L-ASNase were able to self-assemble with PLL-g-PEG to successfully co-encapsulate both L-ASNase and DOX to form NPs.

3.1—Characterization of PLL-g-PEG Co-polymer using ^{1}H NMR Spectroscopy

The PLL-g-PEG co-polymers were synthesized using 15-30 kDa PLL, 2 kDa mPEG NHS, and 5 kDa MAL-PEG-NHS. The starting materials and the co-polymer were characterized using ^{1}H NMR spectroscopy to confirm successful co-polymer synthesis. Figure 12 shows the molecular structure of PLL-g-PEG.

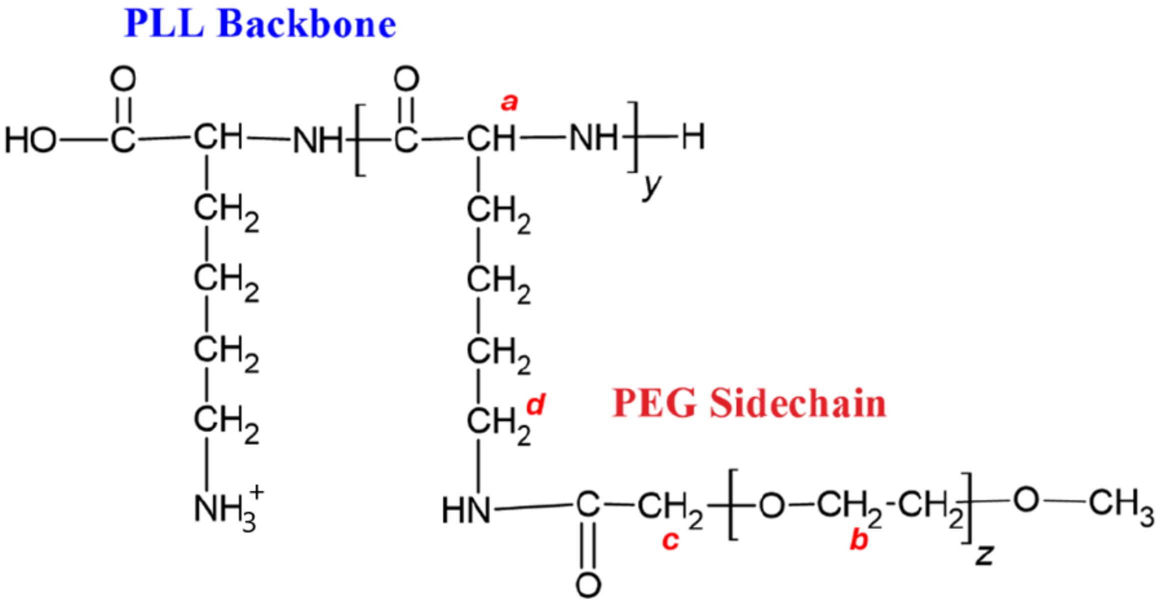

Figure 12 Molecular structure of PLL-g-PEG. *a* (-CHC(O)NH-), *b* (–OCH_2CH_2–), *c* (–$OCH_2C(O)NH$–,), *d* (–$CH_2NHC(O)CH_2$–).

Figures 13, 14, and 15 show ^{1}H NMR spectra of PEG, PLL, and PLL-g-PEG, respectively. The strong peak 3.6 – 3.7 ppm arises from the protons of the PEG repeating unit (strong, –OCH_2CH_2–, *b*) [63], which is clearly visible in Figures 13 and 15. The peak 4.2 – 4.3 ppm (medium,-CHC(O)NH–, *a*) corresponds to the proton on the lysine backbone in PLL and is observed in both Figures 14 and 15. The peak 2.5 ppm (medium, –$OCH_2C(O)NH$–, *c*) confirms the PEG-lysine linkage. The peak 3.4 ppm (medium, –$CH_2NHC(O)CH_2$–, *d*) represents the other side of the PEG-lysine linkage [63][64]. These peaks confirm the PEG grafting onto PLL compared to the individual PLL and PEG spectra.

The grafting ratio of each PLL-g-PEG was determined using ^{1}H NMR. Each grafting ratio is an approximation as a distribution of PLL molecular weights was used to synthesize the grafted copolymer. The grafting ratio, or PEG chains per PLL chain, was determined by integrating the PLL and PEG peaks at 4.3 ppm and 3.7 ppm, respectively. A summary of the copolymers produced is shown in Table 2.

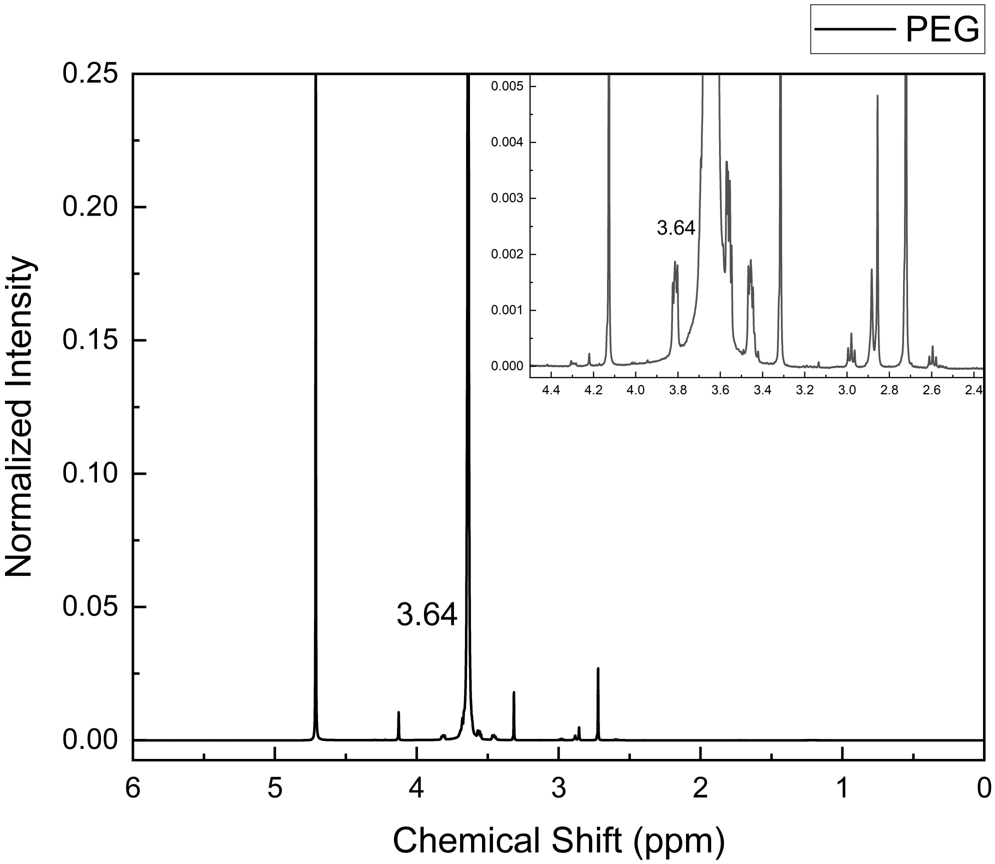

Figure 13 ^{1}H NMR spectrum of PEG in D_2O. *b* ($–OCH_2CH_2–$), 3.64 ppm.

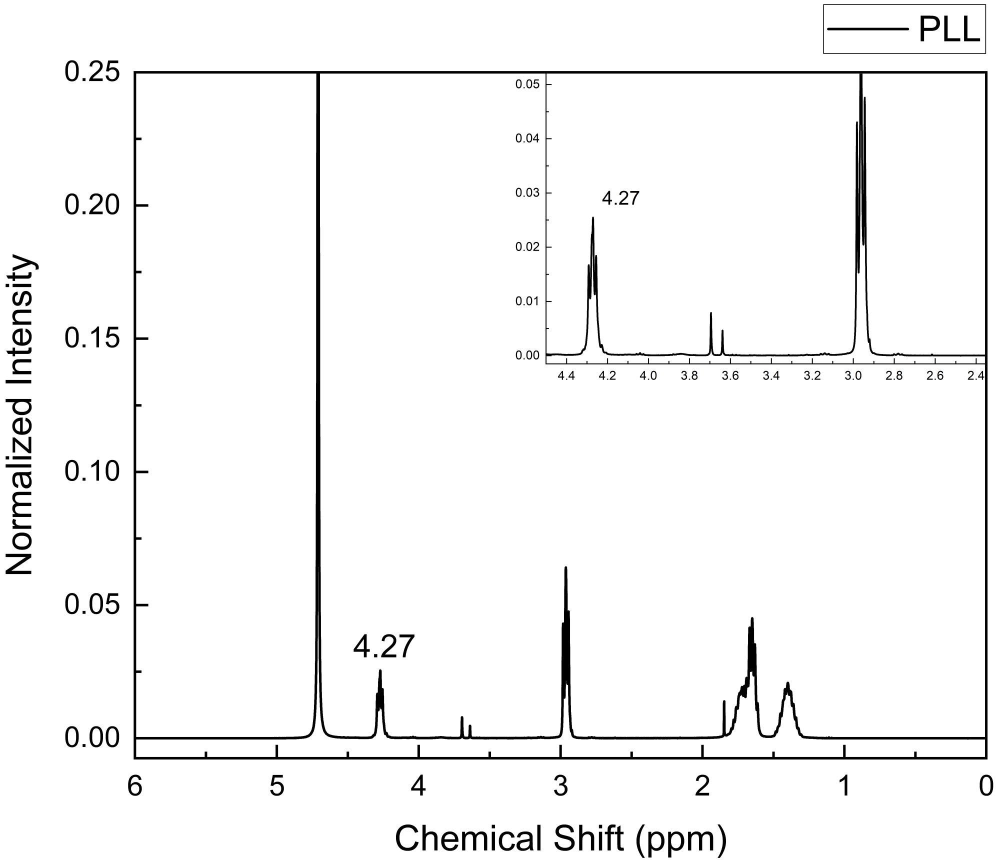

Figure 14 ^{1}H NMR spectrum of PLL in D_2O. *a* (-CHC(O)NH-)), 4.27 ppm.

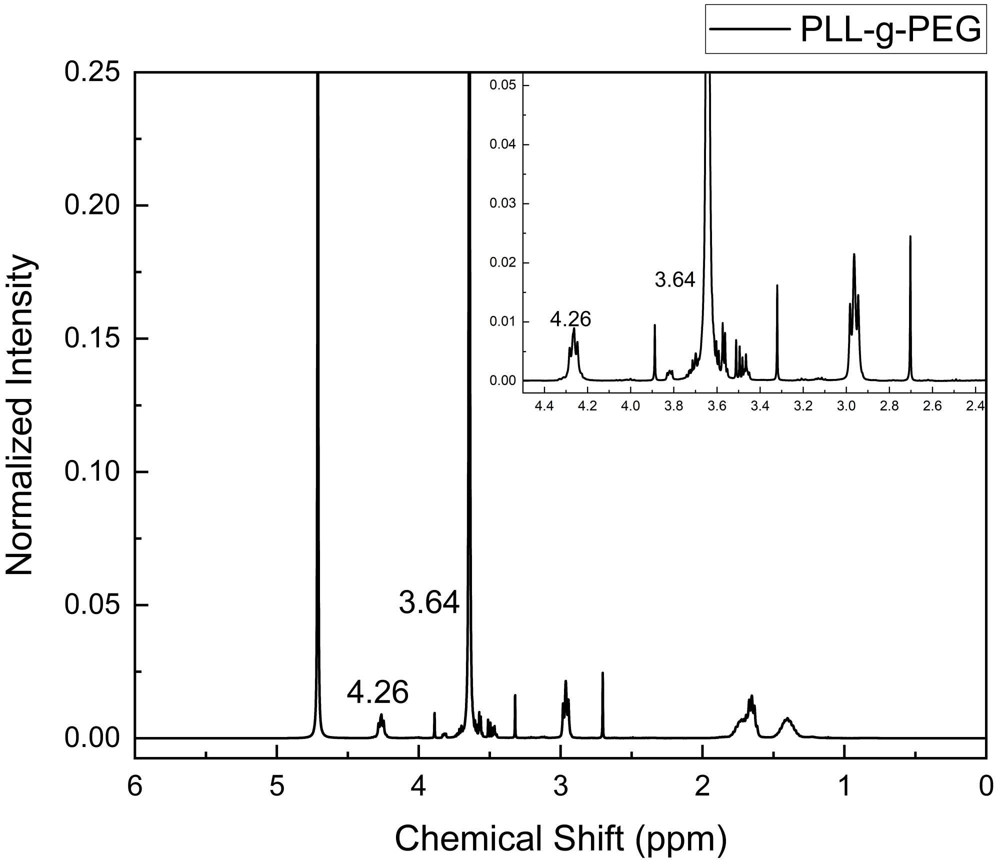

Figure 15 ^{1}H NMR spectrum of PLL-g-PEG in D_2O. *a* (-CHC(O)NH-)), 4.27 ppm; *b* (–OCH_2CH_2–), 3.64 ppm.

Table 2. Determination of grafting ratios for PLL-g-PEG co-polymers.

Co-polymer Sample	Integration of PLL -CH- Peak	Integration of PEG -CH_2CH_2O- Peak	Calculated Grafting Ratio
PLL-g-PEG 1	1.000	36.5950	17.71
PLL-g-PEG 2	1.000	27.3507	13.23
PLL-g-PEG 3	1.000	26.2660	12.71
PLL-g-PEG 4	1.000	21.7139	10.51

3.2—Characterization of PLL-g-PEG Co-polymer using ATR-FTIR Spectroscopy

ATR-FTIR was utilized to further validate the successful synthesis of PLL-g-PEG co-polymers. Distinct peaks at approximately 2900 and 1600 cm^{-1} in the PLL spectrum correspond to -NH- stretching and -NH- bending vibration characteristics of PLL, respectively [65]. The PEG spectra exhibit two well-defined peaks at approximately 2800 cm^{-1} and 1050 cm^{-1}. These peaks are associated with -CH- stretching and -COC- vibration, respectively [66]. The co-polymer spectrum displays strong characteristic PEG -CH- and -COC- functional group peaks. The peak associated with -NH- bending vibrations in PLL is diminished significantly. Many free primary amines are converted to amides, potentially causing a decrease in peak intensity [67]. This decrease could be attributed to the grafting ratio, where numerous PEG units are attached to each PLL unit, resulting in reduced peak intensities associated with PLL due to increased shielding from PEG. The presence of characteristic peaks from both PLL and PEG spectra in the PLL-g-PEG spectrum confirms successful co-polymer synthesis. The attenuation of the PLL peak intensity in the co-polymer spectrum provides additional support for a grafting ratio with multiple PEG units attached to each PLL unit.

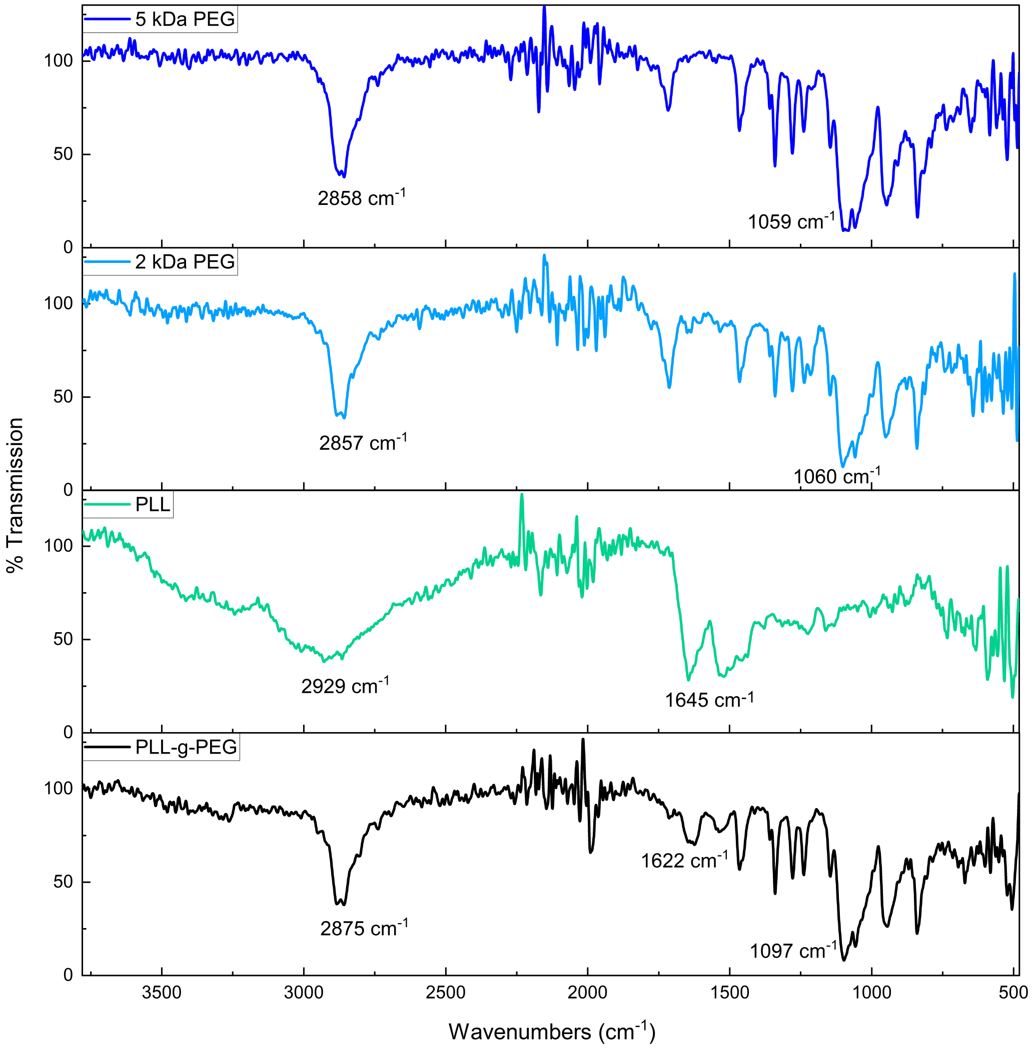

Figure 16 ATR-FT-IR spectra of 15 – 30 kDa PLL, 2 kDa, PEG, 5 kDa PEG, and PLL-g-PEG co-polymer 4. PLL, -NH- stretching, 2929 cm^{-1}, -NH- bending, 1646 cm^{-1}; 2 kDa PEG, -CH- stretching, 2857 cm^{-1}, -COC- vibration, 1060 cm^{-1}; 5 kDa PEG, -CH- stretching, 2858 cm^{-1}, -COC- vibration, 1059 cm^{-1}; PLL-g-PEG, -CH- stretching, 2875 cm^{-1}, -NH- bending, -COC- vibration, 1622 cm^{-1}, 1097 cm^{-1}.

3.3—Confirmation of BSA-DOX Conjugation using UV-Vis and ATR-FTIR spectroscopies

UV-Vis spectroscopy was employed to verify the successful conjugation of DOX to primary amine groups present on the lysine residues located on the surface of BSA. Successful conjugation is confirmed by a redshift in the maximum absorbance of the DOX spectrum, shifting from 482 nm to approximately 500 nm [53]. This redshift could be the result of multiple factors. The primary amine can react with the carbonyl to form a double bond, resulting in a Schiff base [68]. Conjugating DOX to BSA also changes the environment around DOX, causing different intermolecular interactions, such as increased or decreased hydrogen bonding [69]. It could also change the electrostatic interactions present in the molecule, altering its ground energy state [70]. The characteristic protein absorbance peak for BSA at 280 nm has also affected upon functionalization with multiple DOX molecules, with a corresponding redshift observed in its spectrum, shifting the maximum absorbance of 280 nm to approximately 290 nm. This is evident in the BSA-DOX conjugates spectrum, shown above. However, the broad curves observed in the spectrum suggest BSA proteins with low DOX conjugation and unattached DOX molecules. These redshifts suggest the successful conjugation of DOX to the surface of BSA through the reducible linker DTSSP.

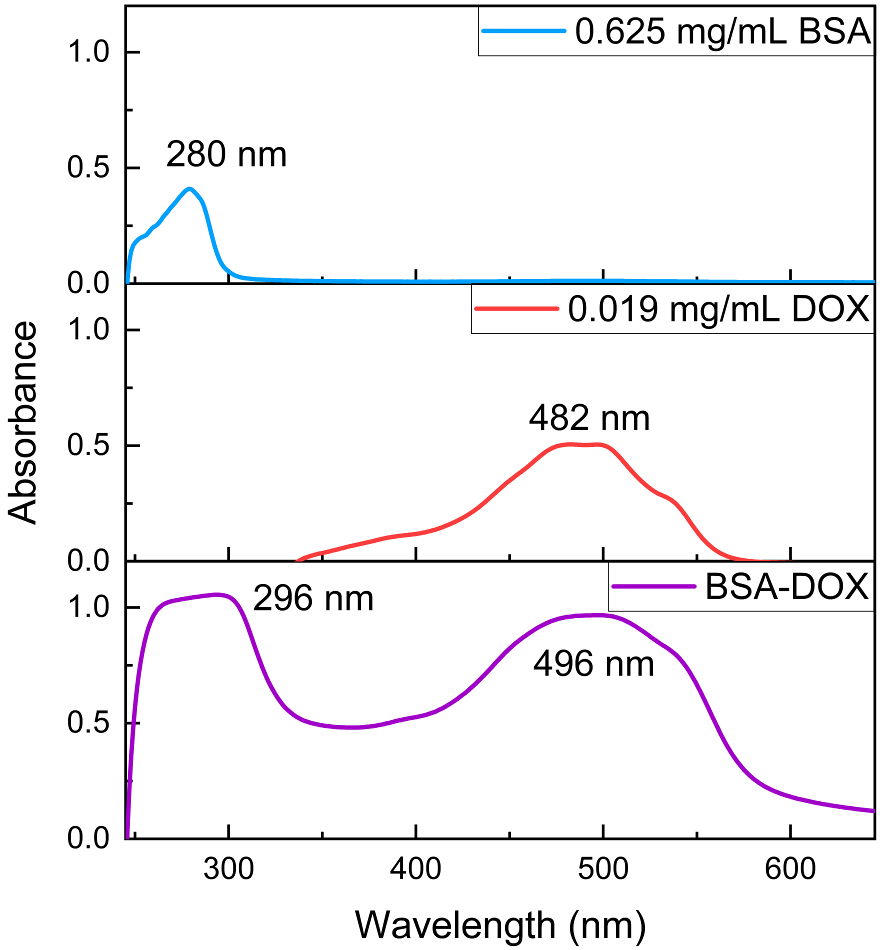

Figure 17 UV-Vis spectra of 0.625 mg/mL BSA, 0.019 mg/mL DOX, and BSA-DOX conjugates. BSA, maximum absorbance, 280 nm; DOX, maximum absorbance, 482 nm; BSA-DOX, maximum absorbances, 296 nm and 496 nm.

FTIR spectra were evaluated for DOX, BSA, DTSSP, and the BSA-DOX conjugates to confirm the synthesis of BSA-DOX conjugates. The BSA spectrum exhibits three prominent peaks at approximately 3280 cm^{-1}, 1650 cm^{-1}, and 1520 cm^{-1} that are associated with -OH stretching vibrations, -C=O- vibrational modes, and -NH- bending vibrations, respectively [71]. The peak 1650 cm^{-1} in the DTSSP spectrum is attributable to -C=O- vibrations. The DOX spectrum shows two principal peaks at approximately 2980 cm^{-1} and 1060 cm^{-1}, which overlap with corresponding peaks in the DTSSP spectrum. The peak 1060 cm^{-1} is attributed to -CO- vibrations, whereas the peak 2980 cm^{-1} corresponds to -CH- stretching vibrations [71][73]. These peaks are also evident in the BSA-DOX conjugates spectrum. However, the substantial overlap between them makes it difficult to determine from which material each peak is originating. But the presence of peaks 1060, 1518, 1645, 2988, and 3290 cm^{-1}, which are originating from the starting materials, suggest a successful conjugation.

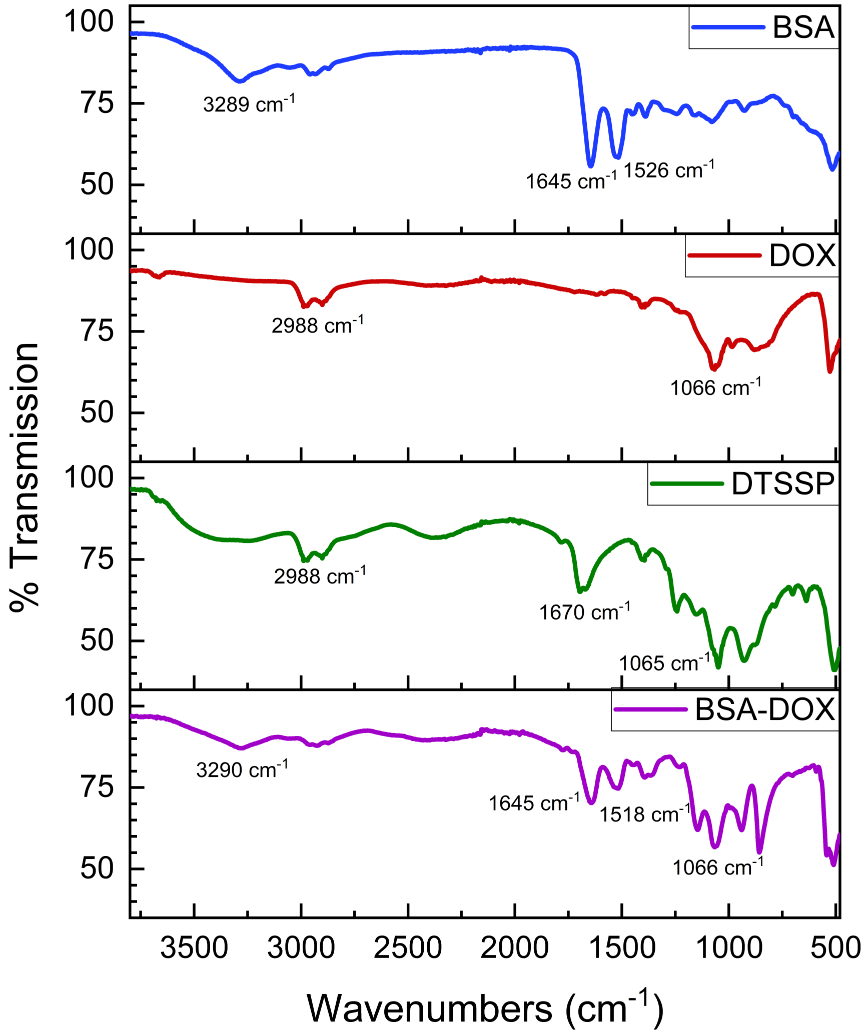

Figure 18 ATR-FT-IR spectra of BSA, DTSSP, DOX, and BSA-DOX conjugates. BSA, -OH- stretching, 3289 cm^{-1}, -C=O- vibrational modes, 1645 cm^{-1}, -NH- bending vibrations, 1526 cm^{-1}; DOX, -CH- stretching, 2988 cm^{-1}, -CO- vibrations, 1060 cm^{-1}; DTSSP, -CH- stretching, 2988 cm^{-1}, -C=O- vibrational modes, 1670 cm^{-1}, -CO- vibrations, 1065 cm^{-1}; BSA-DOX, -OH- stretching, 3290 cm^{-1}, -C=O- vibrational modes, 1645 cm^{-1}, -NH- bending, 1518 cm^{-1}, -CO- vibrations, 1066 cm^{-1}.

3.4—Evaluation of BSA-DOX Conjugation using SDS-PAGE

SDS-PAGE was utilized to assess the impact of DOX conjugation on BSA. Figure 19 shows that free BSA (0.266 mg/mL) migrates to approximately 55 kDa in lane 3. Lane 4 shows DOX, which is not detectable as anticipated on a PAGE gel because coomassie blue would be unlikely to bind this molecule, and it has a very small size that would most likely run off the gel. Lanes 5–8 display four independently synthesized samples diluted to 0.266 mg/mL of BSA-DOX conjugates. BSA-DOX conjugates showed broader bands 55 kDa with light smearing. BSA appears to be bleeding over into lane 4. The smearing and band observed in lane 4 appears to indicate that this gel was overloaded. In future gels, lower concentrations of BSA and BSA-DOX conjugates will be needed for accurate evaluation of DOX conjugation. Light bands appear in lanes 5 - 8 around approximately 38 - 40 kDa. DOX conjugation could have potentially disrupted BSA stability in a small number of proteins, causing light bands to appear at a lower molecular weight. This data does suggest that the conjugation of DOX slightly affected the mobility of BSA on the gel.

Figure 19 SDS-PAGE (12%) gel of BSA-DOX conjugates. Lane 2: Molecular Weight Ladder, Lane 3: 0.266 mg/mL free BSA, Lane 4: 0.266 mg/mL free DOX, Lane 5: 0.266 mg/mL BSA-DOX 1, Lane 6: 0.266 mg/mL BSA-DOX 2, Lane 7: 0.266 mg/mL BSA-DOX 3, Lane 8: 0.266 mg/mL BSA-DOX 4.

3.5—Synthesis of L-ASNase, L-ASNase/DOX, and L-ASNase/BSA-DOX NPs

Three different types of NPs were synthesized using L-ASNase and DOX. Co-encapsulations were done using L-ASNase/DOX and L-ASNase/BSA-DOX to synthesize two different types of NPs. In all three types of NPs the proteins/DOX were encapsulated within PLL-g-PEG co-polymers to achieve NPs through electrostatic interactions. The isoelectric points of L-ASNase from E. coli and BSA are pH 4.6 - 5.5 and pH 5, respectively [36][58]. Hence, at a pH of 7.4, both L-ASNase and BSA carry a net negative charge density on the surface of these proteins. Positive charges on the PLL backbone play a key role in the formation of NPs by electrostatically interacting with these negatively charged protein molecules. Figure 20 shows a schematic diagram of the synthesis of L-ASNase/BSA-DOX encapsulated PLL-g-PEG NPs.

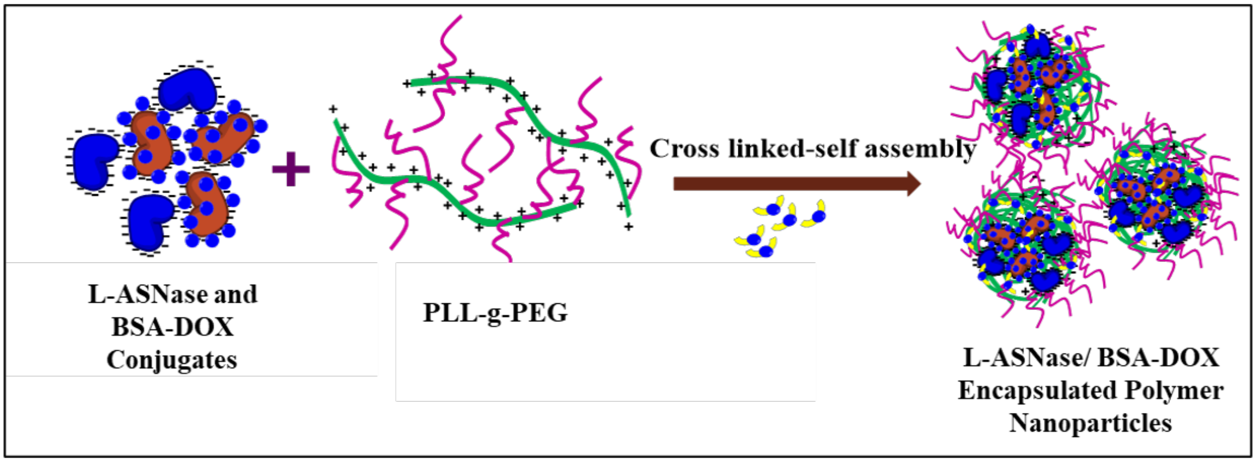

Figure 20 A schematic diagram of synthesis of L-ASNase/BSA-DOX encapsulated PLL-g-PEG NPs.

Following protein encapsulation, NPs were crosslinked with Glu. and/or DTSSP. The crosslinking reaction occurs between free primary amine groups left on the co-polymer chains and the specific functional groups of the linker molecules. In Glu. crosslinking, the two carbonyl groups on Glu. react with primary amines to form what's commonly known as a 'Schiff' base [74][75]. In DTSSP crosslinking, the two NHS ester groups on DTSSP react with primary amines to form am amide bond [61]. Glu. and DTSSP crosslinks help retain the encapsulated proteins within the NP complex.

3.6—Physicochemical Characterization of NPs

DLS was used to evaluate the average hydrodynamic diameter and PDI. The DLS technique measures time-dependent fluctuations of light intensity signal scattered by particles undergoing Brownian motion in a suspension. The autocorrelation function (ACF) of the scattering intensity for monodisperse particles decays exponentially with a decay rate that is proportional to the diffusion coefficient of the particle motion, which, in turn, is related to the hydrodynamic particle diameter, via the Stokes-Einstein relation [76][77]. NPs are typically described as particles in the size range of 1 to 1,000 nm. Another crucial measurement provided by DLS is the PDI. The PDI provides information into the breadth of the size distribution of particles within a solution, such as the variability of particle sizes. The PDI ranges from 0.1 to 1, with values closer to 0.1 indicating a narrow size distribution with low size variability. Conversely, values approaching 1 reflect a broader size distribution with high size variability. We aim to synthesize NPs with an optimal size range of approximately 100 nm and PDI values closer to 0.1. As stated in our experimental chapter, two types of co-encapsulated NPs were synthesized. The first type co-encapsulated free DOX and L-ASNase, while the second type co-encapsulated BSA-DOX conjugates and L-ASNase. These NPs were crosslinked with Glu. and DTSSP crosslinkers. DLS measurements were done on each set of NPs in triplicate samples. The Z-average hydrodynamic diameters for each type of co-encapsulated NPs are provided in Table 3. Figure 21 illustrates the average hydrodynamic diameter for each type of co-encapsulated NPs, along with the respective linker. A significant difference in the average hydrodynamic diameter was observed between /L-ASNase/DOX co-encapsulated NPs and L-ASNase/BSA-DOX NPs. Specifically, free L-ASNase/DOX NPs exhibited average hydrodynamic diameters of 415.3 ± 344.8 nm, whereas L-ASNase/BSA-DOX NPs showed 84.8 ± 48.0 nm. This finding indicates that co-encapsulation with free DOX results in substantially larger NPs, whereas incorporating BSA-DOX conjugates allows for the synthesis of smaller NPs. A corresponding difference in the mean PDI was also observed, as shown in Figure 22. The average PDI was approximately 0.689 ± 0.002 for L-ASNase/DOX NPs and

0.321 ± 0.001 for L-ASNase/BSA-DOX NPs, indicating that using BSA-DOX conjugates reduces the size variability of the produced NPs. Since free DOX possesses a neutral charge, it does not contribute to the self-assembly of NPs. High concentrations of free DOX may disrupt close interactions between L-ASNase and co-polymer, promoting the formation of larger NPs. However, the negative surface charge of BSA allows BSA-DOX conjugates to effectively participate in NP self-assembly alongside L-ASNase without compromising the interactions essential for L-ASNase co-encapsulation.

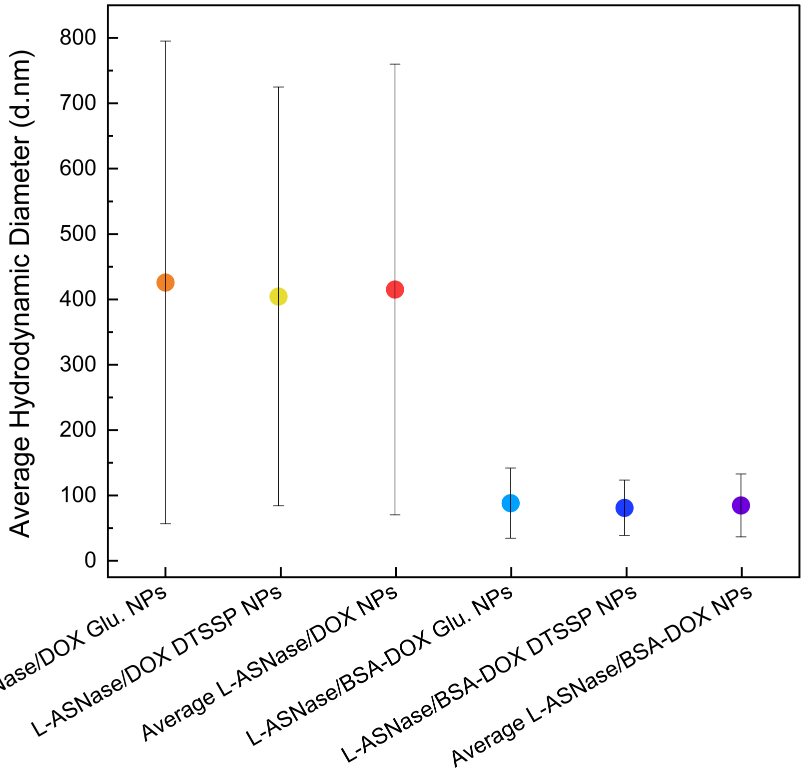

Figure 21 Distribution profile of average hydrodynamic diameters of L-ASNase/DOX NPs and L-ASNase/BSA-DOX NPs. L-ASNase/DOX Glu. NPs, z-avg., 394.5 ± 339.2 nm; L-ASNase/DOX DTSSP NPs, z-avg., 404.6 ± 320.4 nm; Average L-ASNase/DOX NPs, z-avg., 415.3 ± 344.8 nm; L-ASNase/BSA-DOX Glu. NPs, z-avg., 88.3 ± 53.8 nm; L-ASNase/BSA-DOX DTSSP NPs, z-avg., 81.2 ± 42.3 nm; Average L-ASNase/BSA-DOX NPs, z-avg., 84.8 ± 48.0 nm.

Table 3. Hydrodynamic diameter and PDI for NPs.

NPs Description	Average Hydrodynamic Diameter (d.nm)	Average PDI
L-ASNase/DOX Glu. NPs 1	426.0 ± 369.3	0.751 ± 0.008
L-ASNase/DOX Glu. NPs 2	414.4 ± 363.9	0.771 ± 0.008
L-ASNase/DOX Glu. NPs 3	343.2 ± 286.1	0.695 ± 0.008
Average L-ASNase/DOX Glu. NPs	394.5 ± 339.2	0.739 ± 0.001
L-ASNase/DOX DTSSP NPs 1	443.7 ± 344.1	0.602 ± 0.008
L-ASNase/DOX DTSSP NPs 2	373.2 ± 279.3	0.560 ± 0.003
L-ASNase/DOX DTSSP NPs 3	396.9 ± 336.8	0.720 ± 0.015
Average L-ASNase/DOX DTSSP NPs	404.6 ± 320.4	0.627 ± 0.003
L-ASNase/BSA-DOX Glu. NPs 1	73.0 ± 45.7	0.392 ± 0.003
L-ASNase/BSA-DOX Glu. NPs 2	94.7 ± 56.9	0.3615 ± 0.003
L-ASNase/BSA-DOX Glu. NPs 3	97.3 ± 58.4	0.361 ± 0.004
Average L-ASNase/BSA-DOX Glu. NPs	88.3 ± 53.8	0.371 ± 0.001
L-ASNase/BSA-DOX DTSSP NPs 1	104.1 ± 52.9	0.258 ± 0.007
L-ASNase/BSA-DOX DTSSP NPs 2	77.5 ± 41.4	0.286 ± 0.001
L-ASNase/BSA-DOX DTSSP NPs 3	62.0 ± 32.1	0.268 ± 0.005
Average L-ASNase/BSA-DOX DTSSP NPs	81.2 ± 42.3	0.271 ± 0.001
Overall Average L-ASNase/DOX NPs (irrespective of the crosslinker used)	415.3 ± 344.8	0.689 ± 0.002
Overall Average L-ASNase/BSA-DOX NPs (irrespective of the crosslinker used)	84.8 ± 48.0	0.321 ± 0.001

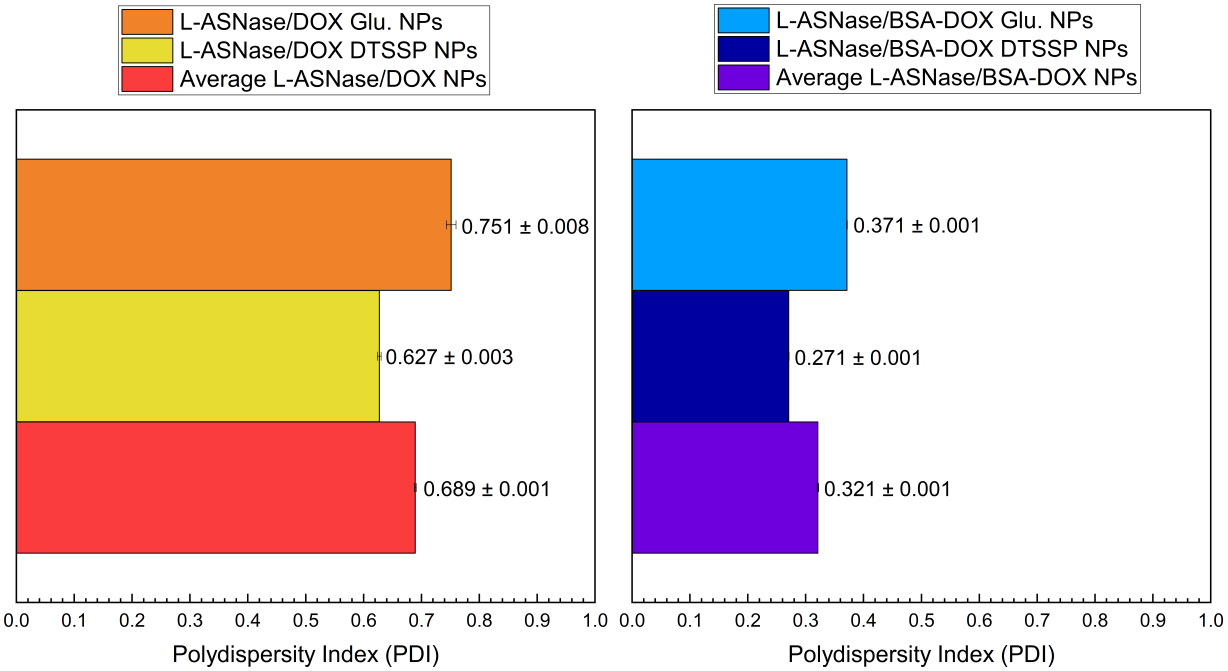

Figure 22 PDIs of L-ASNase/DOX NPs and L-ASNase/BSA-DOX NPs. L-ASNase/DOX Glu. NPs, z-avg., 0.739 ± 0.001; L-ASNase/DOX DTSSP NPs, z-avg., 0.627 ± 0.003; Average L-ASNase/DOX NPs, z-avg., 0.689 ± 0.002; L-ASNase/BSA-DOX Glu. NPs, z-avg., 0.371 ± 0.001; L-ASNase/BSA-DOX DTSSP NPs, z-avg., 0.271 ± 0.001; Average L-ASNase/BSA-DOX NPs, z-avg., 0.321 ± 0.001.

Zeta potential describes the potential difference between the dispersion solvent (slipping plane) and the stationary layer of fluid at the particle surface (stern layer), as illustrated by Figure 23, thereby reflecting the overall surface charge of particles in solution [78]. PALS is a technique used to measure zeta potential by applying an electric field to a particle suspension and analyzing the resultant Doppler shift in the scattered light determined through the Gaussian interactions [78]. These frequency shifts are compared against a reference beam to calculate the average zeta potential of the particles.

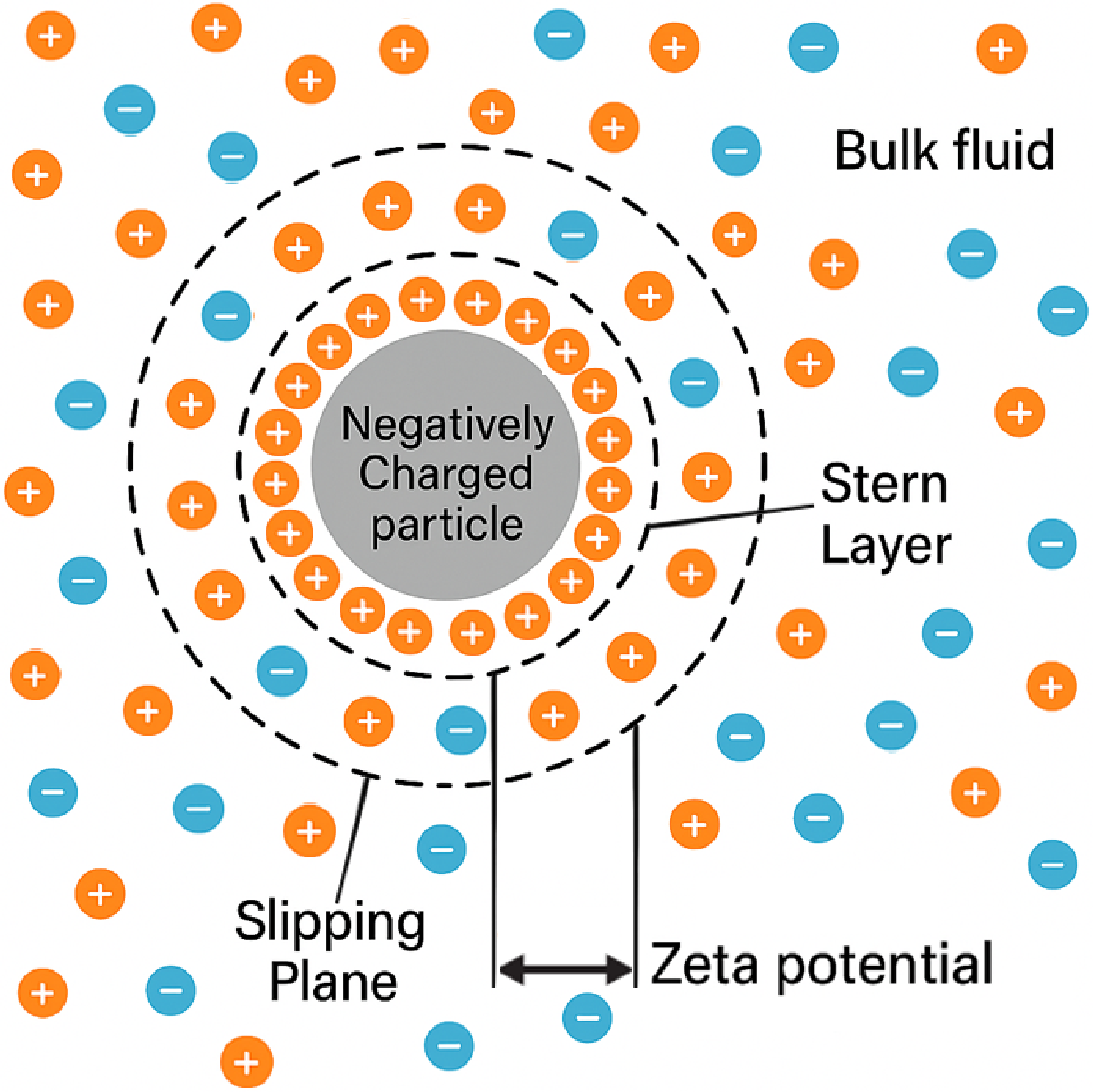

Figure 23 Zeta potential diagram. This illustrates the slipping plane and stern layer used to determine the zeta potential. In this example, the NP is negatively charged and tightly surrounded by positive ions (yellow), with negative ions (blue) more dispersed.

Table 4. Zeta potential (mV) of NPs.

NPs Description	Average Zeta Potential (mV)
L-ASNase/DOX Glu. NPs 1	5.96 ± 0.933
L-ASNase/DOX Glu. NPs 2	5.21 ± 0.501
L-ASNase/DOX Glu. NPs 3	6.85 ± 0.655
Average L-ASNase/DOX Glu. NPs	6.01 ± 0.022
L-ASNase/DOX DTSSP NPs 1	8.01 ± 1.330
L-ASNase/DOX DTSSP NPs 2	8.15 ± 0.734
L-ASNase/DOX DTSSP NPs 3	8.26 ± 0.452
Average L-ASNase/DOX DTSSP NPs	8.14 ± 0.033
L-ASNase/BSA-DOX Glu. NPs 1	6.04 ± 0.420
L-ASNase/BSA-DOX Glu. NPs 2	3.03 ± 0.313
L-ASNase/BSA-DOX Glu. NPs 3	2.77 ± 0.290
Average L-ASNase/BSA-DOX Glu. NPs	3.95 ± 0.049
L-ASNase/BSA-DOX DTSSP NPs 1	0.843 ± 0.746
L-ASNase/BSA-DOX DTSSP NPs 2	3.47 ± 0.739
L-ASNase/BSA-DOX DTSSP NPs 3	1.34 ± 0.753
Average L-ASNase/BSA-DOX DTSSP NPs	1.88 ± 0.038
Overall Average L-ASNase/DOX NPs (irrespective of the crosslinker used)	7.07 ± 0.021
Overall Average L-ASNase/BSA-DOX NPs (irrespective of the crosslinker used)	2.92 ± 0.020

The average zeta potential was measured for each set of NPs. Table 4 lists the measured zeta potential for all sets of NPs. Figure 24 presents a comparison of the overall average zeta potential of L-ASNase/DOX NPs and L-ASNase/BSA-DOX NPs. L-ASNase/DOX NPs exhibited an average zeta potential of 7.07 mV ± 0.02, significantly higher than the 2.92 mV ± 0.02 observed for L-ASNase/BSA-DOX NPs. This may be caused by the differences in encapsulated protein concentrations. The L-ASNase/DOX NPs incorporate a single type of negatively charged protein, whereas the L-ASNase/BSA-DOX NPs have a higher concentration of negatively charged proteins due to BSA. BSA is also a smaller protein than L-ASNase, meaning it could pack tighter or move closer to the surface of the co-polymer matrix. Furthermore, the observed net positive surface charge of L-ASNase/BSA-DOX NPs suggests that a greater proportion of negatively charged proteins are sequestered within the NP core, while the surface contains primarily cationic co-polymer, causing a net positive surface charge and zeta potential.

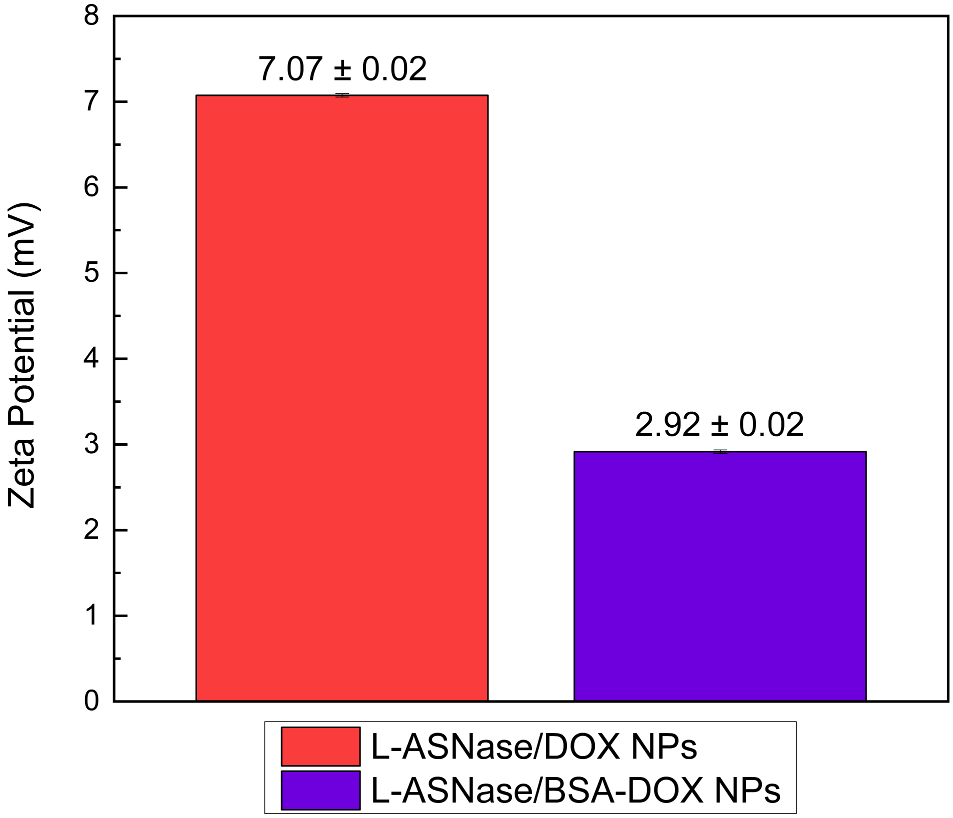

Figure 24 Average zeta potentials of L-ASNase/DOX NPs and L-ASNase/BSA-DOX NPs. Red represents L-ASNase/DOX NPs, and purple represents L-ASNase/BSA-DOX NPs. Average L-ASNase/DOX NPs, zeta potential, 7.07 ± 0.02 mV; Average L-ASNase/BSA-DOX NPs, zeta potential, 2.92 ± 0.02 mV.

3.7—Scanning-Transmission Electron Microscopy (STEM) NPs

STEM was utilized to obtain a comprehensive distribution profile of L-ASNase/DOX NPs and L-ASNase/BSA-DOX NPs. This technique involves focusing an electron beam into a narrow spot at a reduced voltage, which, when directed at a thin sample, enhances electron scattering cross-sections [79]. This method is particularly advantageous for samples lacking heavy atoms because it shows enhanced contrast for materials composed of low atomic number elements. Figure 25 shows STEM images of both,L-ASNase/DOX NPs and L-ASNase/BSA-DOX NPs. Using the STEM images along with the software ImageJ, NP sizes were measured individually, and distribution profiles were developed for both types of NPs. Figure 26 displays a broad size distribution ranging from 0 to 450 nm. The highest frequency of NPs is shown to be between 50 – 100 nm. However, there is a larger variability in sizes, with each group from 0 – 200 nm showing higher frequencies. This suggested that the L-ASNase/DOX NPs are not consistently formed in one set range but primarily fall around sizes close to 100 nm. This size is much smaller than the DLS data. This is most likely due to a combination of swelling and centrifugation. These samples were heavily centrifuged for STEM to ensure that large aggregates did not disrupt NP visibility. In contrast, the distribution profile in Figure 27 for L-ASNase/BSA-DOX NPs is narrower. A pronounced frequency within the 50 – 100 nm range for L-ASNase/BSA-DOX NPs indicates that the majority of NPs synthesized fall within this optimal range. This analysis is almost identical to the DLS data obtained for the same samples. This further supports that BSA-DOX conjugates are more effective at facilitating the formation of self-assembly NPs.

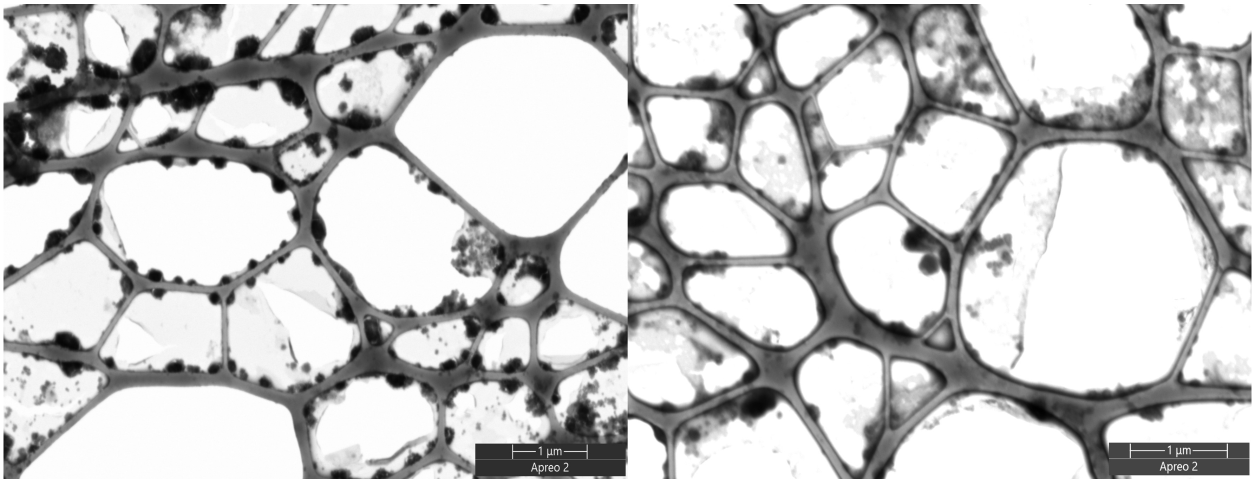

Figure 25 STEM images of L-ASNase/DOX NPs (Left) and L-ASNase/BSA-DOX NPs (Right). A voltage of 30 kV and current of 50 pA were used.

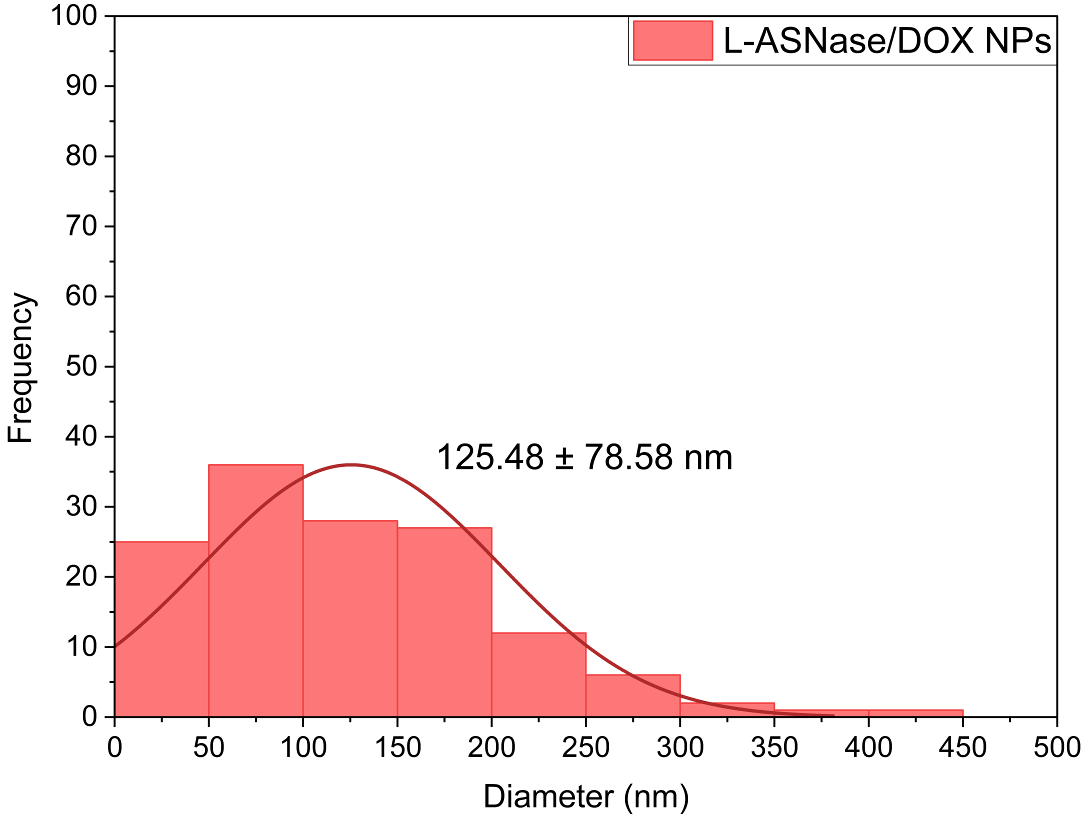

Figure 26 STEM distribution profile of L-ASNase/DOX NPs L-ASNase/DOX NPs, mean diameter, 125.48 ± 78.58 nm. The distribution profile extends from 0 to 450 nm and was developed with 140 individually measured NPs.

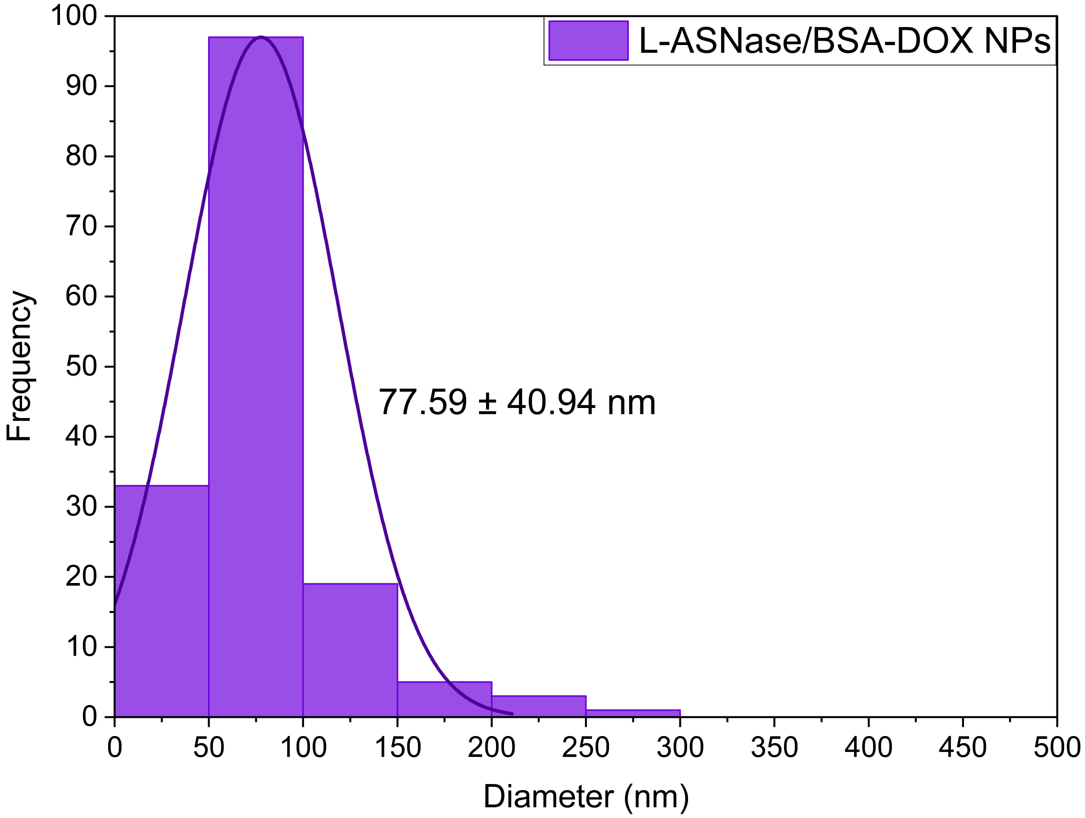

Figure 27 STEM distribution profile of L-ASNase/BSA-DOX NPs. L-ASNase/BSA-DOX NPs, mean diameter, 77.59 ± 40.94 nm. The distribution profile extends from 0 to 300 nm and was developed with 150 individually measured NPs.

3.8—Evaluation of Protein Encapsulation by SDS-PAGE

An SDS-PAGE (12%) gel retardation assay was used to evaluate L-ASNase protein encapsulation. This technique is a highly effective method for the separation of proteins and complex mixtures. The assay denatures proteins both on the NP surface and in solution, allowing unencapsulated proteins to migrate through the gel and appear at positions corresponding to their molecular weights [80]. Figures 28-31 display samples of L-ASNase/DOX Glu. NPs, L-ASNase/DOX

DTSSP NPs, L-ASNase/BSA-DOX Glu. NPs and L-ASNase/BSA-DOX DTSSP NPs, respectively. A clearly defined molecular weight ladder is visible in lane 2 of Figures 27-30 with molecular weight bands of 250, 130, 100, 70, 55, 35, 25, and 10 kDa.

L-ASNase has four identical monomers associated into a tetrameric structure that can more accurately be described as a dimer of dimers with a molecular mass of approximately 120 to 160 kDa possessing antitumor activity. The molecular weight of the L-ASNase is found to vary according to the source of the enzyme. The functional L-ASNase from E. coli is a homotetramer with a molecular weight of about 142 kDa [81][82][83]. In our laboratory conditions, the L-ASNase Native PAGE gel band ran smaller than expected and appeared closer to 120 kDa [52]. However, in SDS-PAGE, L-ASNase shows subunits around 30-40 kDa. This is evident in lane 3 of all the gel images shown in Figures 28-31. The migration of NP samples in lanes 5-8 was mostly hindered. NPs are expected to run through the gel due to their size and positive surface charge. Since the gel runs negative to positive, our NPs should remain in the stacking region. L-ASNase and/or L-ASNase/BSA encapsulated NPs are bigger than free proteins and are not able to freely migrate down the polyacrylamide gel. These NP bands are present right below the well in the stacker region, as shown in each image.

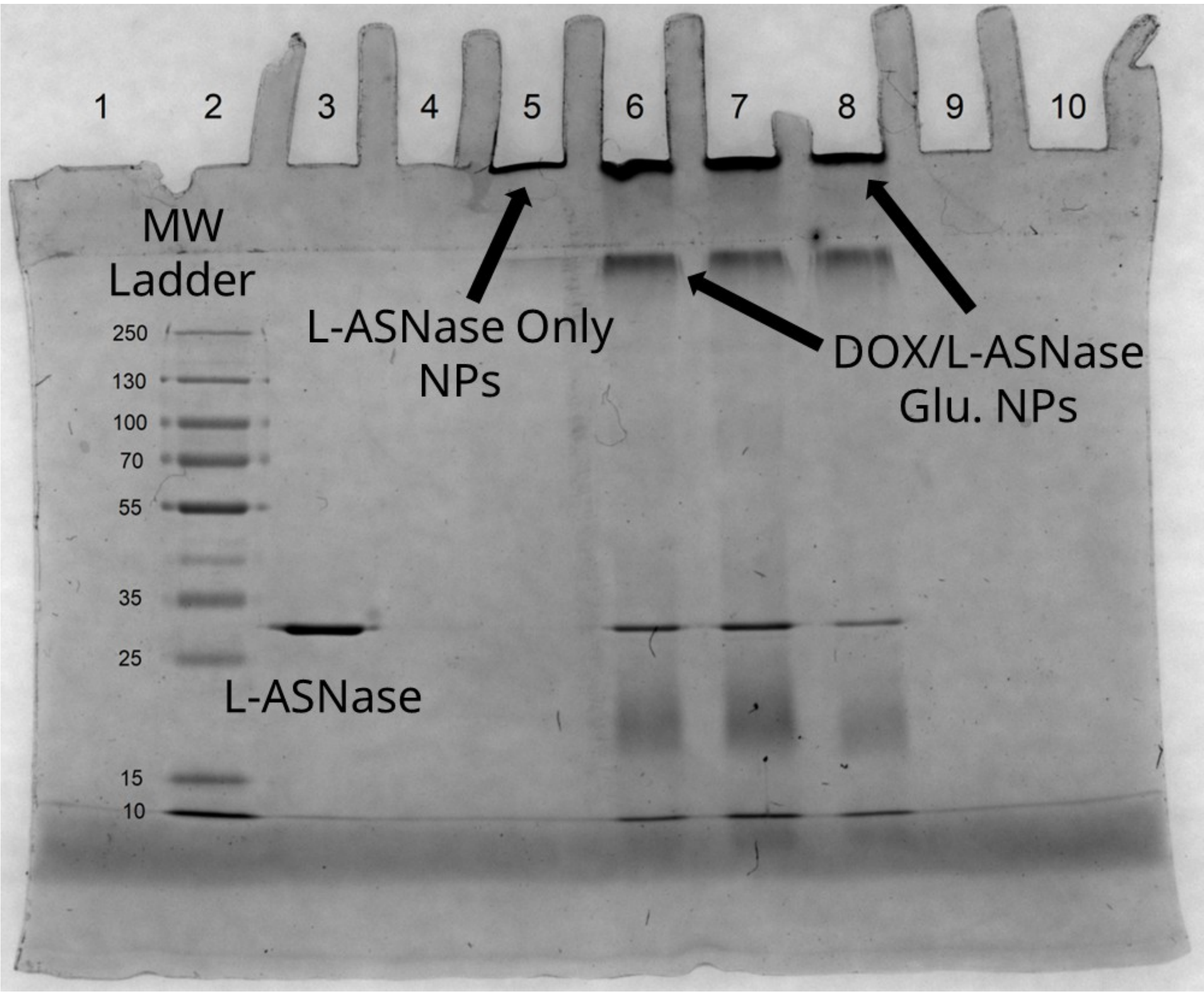

Figure 28 SDS-PAGE (12%) gel of L-ASNase/DOX Glu. NPs. Lane 2: Molecular Weight Ladder, Lane 3: 0.0885 mg/mL free L-ASNase, Lane 4: 0.0885 mg/mL free DOX, Lane 5: L-ASNase Only NPs, Lane 6: L-ASNase/DOX Glu. NPs 1, Lane 7: L-ASNase/DOX Glu. NPs 2, Lane 8: L-ASNase/DOX Glu. NPs 3.

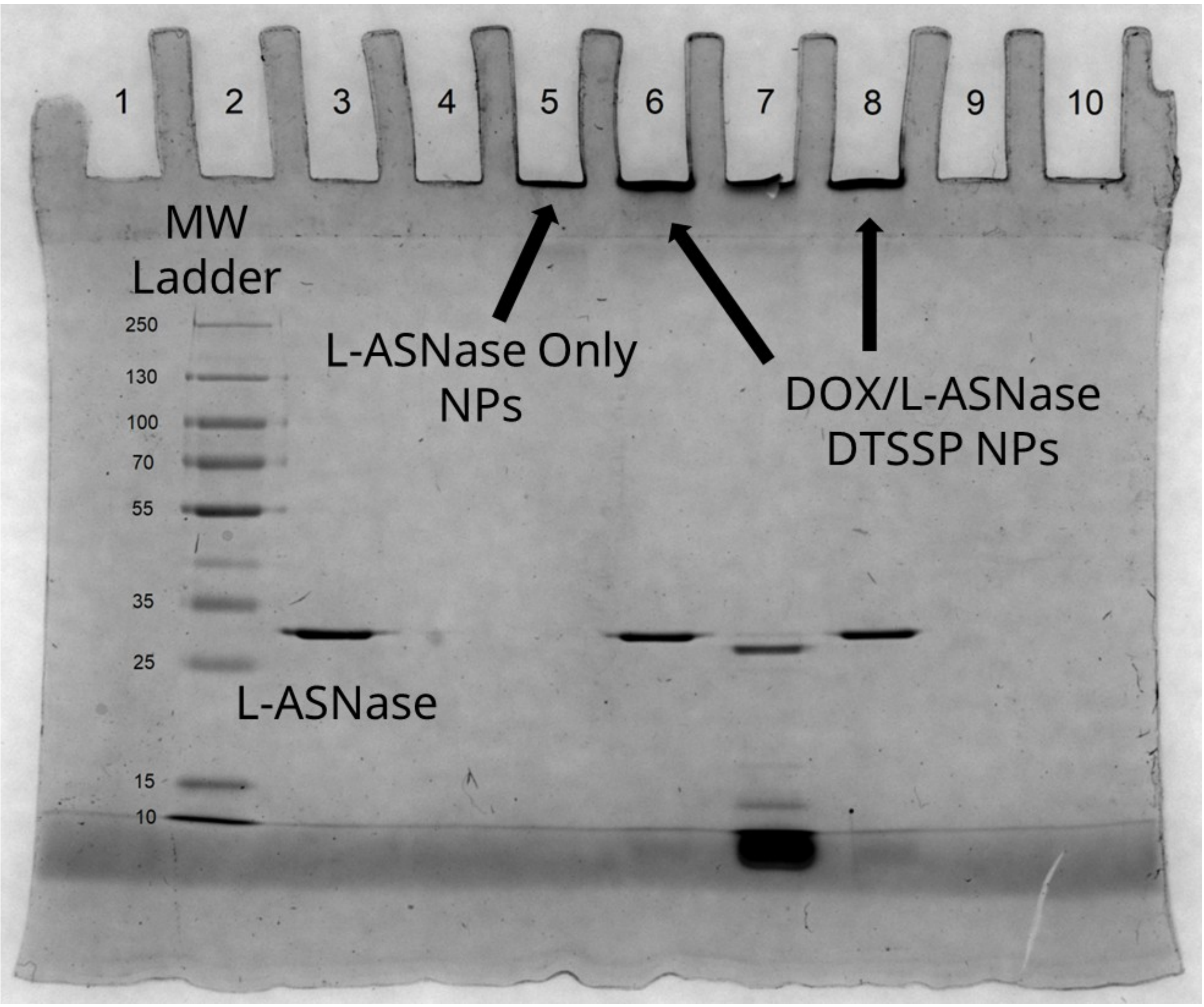

Figure 29 SDS-PAGE (12%) gel of L-ASNase/DOX DTSSP NPs. Lane 2: Molecular Weight Ladder, Lane 3: 0.0885 mg/mL free L-ASNase, Lane 4: 0.0885 mg/mL free DOX, Lane 5: L-ASNase Only NPs, Lane 6: L-ASNase/DOX DTSSP NPs 1, Lane 7: L-ASNase/DOX DTSSP NPs 2, Lane 8: L-ASNase/DOX DTSSP NPs 3.

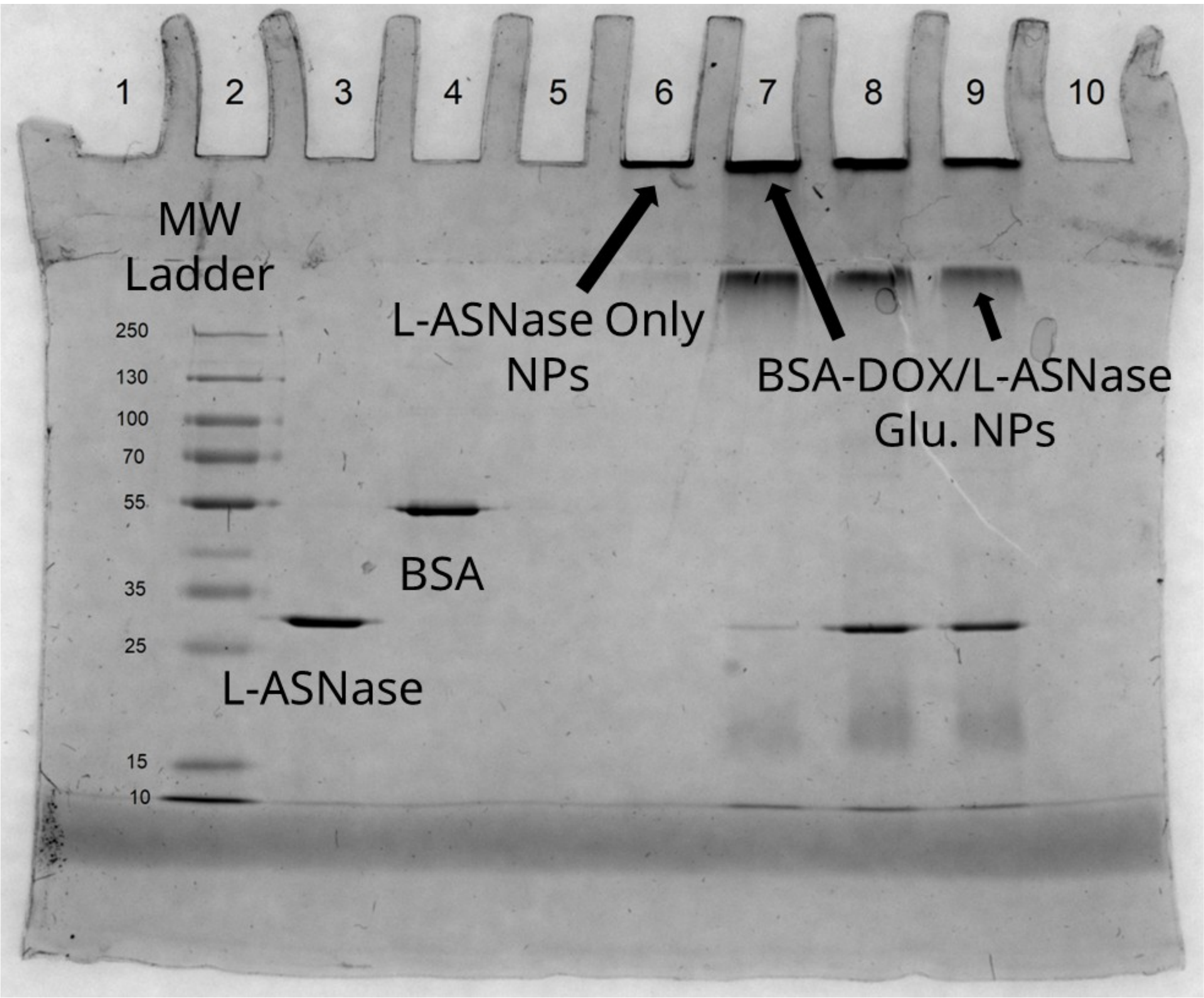

Figure 30 SDS-PAGE (12%) gel of L-ASNase/BSA-DOX Glu. NPs. Lane 2: Molecular Weight Ladder, Lane 3: 0.0885 mg/mL free L-ASNase, Lane 4: 0.0885 mg/mL free BSA, Lane 5: 0.0885 mg/mL free DOX, Lane 6: L-ASNase Only NPs, Lane 7: L-ASNase/BSA-DOX Glu. NPs 1, Lane 8: L-ASNase/BSA-DOX Glu. NPs 2, Lane 9: L-ASNase/BSA-DOX Glu. NPs 3.

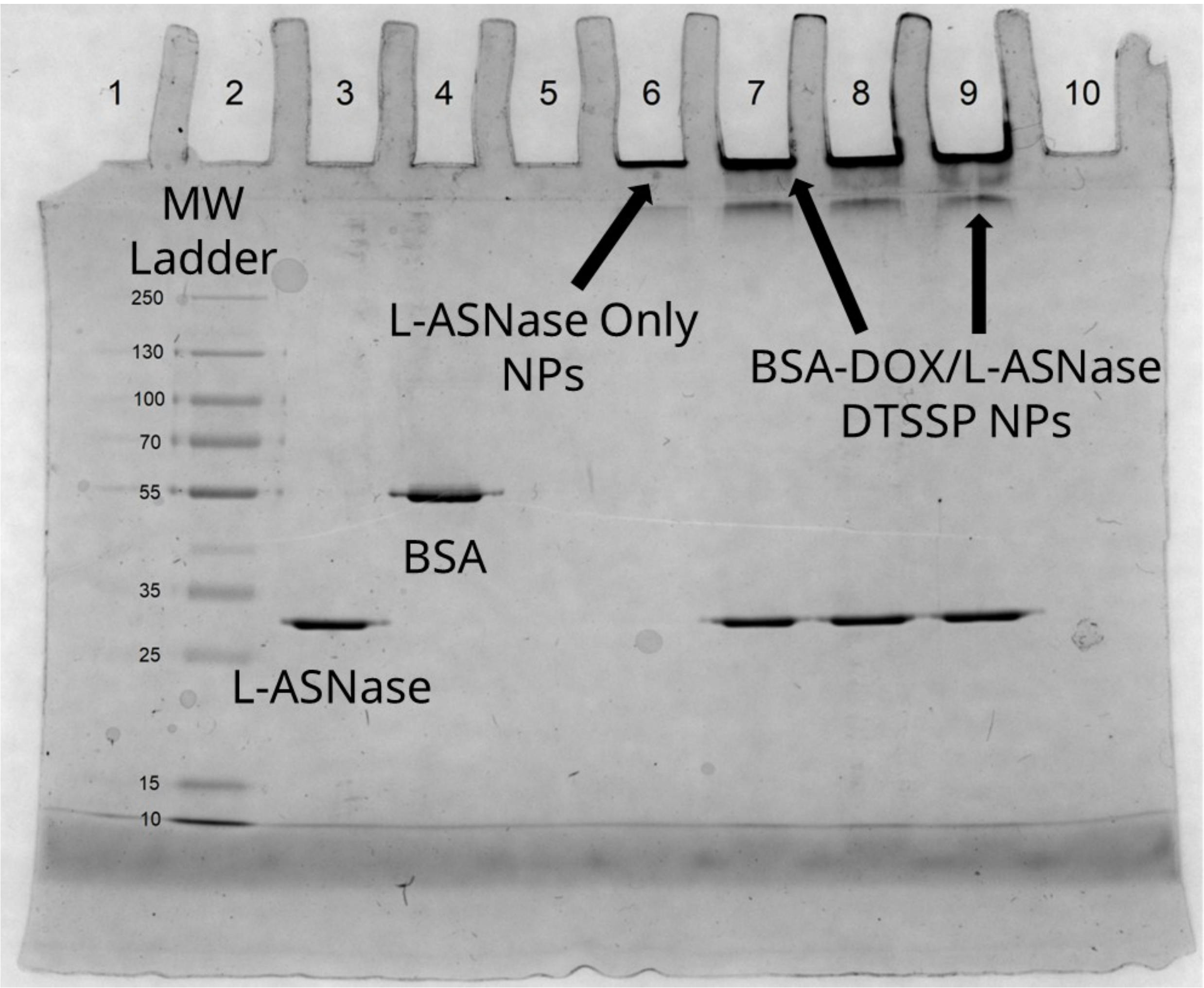

Figure 31 SDS-PAGE (12%) gel of L-ASNase/DOX Glu. NPs. Lane 2: Molecular Weight Ladder, Lane 3: 0.0885 mg/mL L-ASNase, Lane 4: 0.266 mg/mL DOX, Lane 5: L-ASNase Only NPs, Lane 6: L-ASNase/DOX DTSSP NPs 1, Lane 7: L-ASNase/DOX DTSSP NPs 2, Lane 8: L-ASNase/DOX DTSSP NPs 3.

The band resulting from free L-ASNase (shown in lane 3 of each gel) served as the positive control and was used as the reference for quantifying un-encapsulated L-ASNase present in NP preparations. Image Lab software on the gel imager was used to quantify the un-encapsulated L-ASNase present in each NP preparation as a relative quantity compared to the band in lane 3.

Using the observed pixel intensity of the control band with a known concentration, the Image Lab software will determine relative quantities based on the pixel intensity of sample bands. The relative quantity can provide insight to the extent of successful L-ASNase encapsulation. These values are shown in Table 5. L-ASNase only NPs showed a high encapsulation efficiency, resulting in minimal or undetectable free L-ASNase in the gel.

L-ASNase/DOX NPs samples showed high quantities of un-encapsulated L-ASNase, with an average relative quantity of 0.38 ± 0.12. L-ASNase/BSA-DOX NPs showed an average relative quantity of un-encapsulated L-ASNase to be 0.29 ± 0.09. This value is lower than that observed for L-ASNase/DOX NPs. This observation suggested that when BSA-DOX conjugates are used instead of free DOX, L-ASNase is more effectively encapsulated. Figures 30–31 demonstrate that BSA-DOX is almost entirely encapsulated, with no detectable free BSA-DOX conjugates in those gels. This indicates that BSA-DOX conjugates facilitate more effective self-assembly than L-ASNase and may contribute to lesser encapsulation of L-ASNase. At neutral pH, surface lysine residues are typically protonated through their primary amine, adding a positive surface charge to the protein [84]. Conjugation of DOX to these amine groups neutralizes the positive charge, increasing the overall surface electronegativity of the protein's surface and indirectly enhancing its affinity for the cationic polymer. Overall, the gel retardation results suggested that BSA-DOX conjugates slightly affected the amount of L-ASNase that could be encapsulated (subject to the detectability level of gel bands).

Table 5. Relative quantities of un-encapsulated L-ASNase in NP samples.

NPs Description	Relative Quantities of un-encapsulated L-ASNase
L-ASNase/DOX Glu. NPs 1	0.33
L-ASNase/DOX Glu. NPs 2	0.29
L-ASNase/DOX Glu. NPs 3	0.10
Average L-ASNase/DOX Glu. NPs	0.24 ± 0.12
L-ASNase/DOX DTSSP NPs 1	0.84
L-ASNase/DOX DTSSP NPs 2	0.22
L-ASNase/DOX DTSSP NPs 3	0.47
Average L-ASNase/DOX DTSSP NPs	0.51 ± 0.33
L-ASNase/BSA-DOX Glu. NPs 1	0.06
L-ASNase/BSA-DOX Glu. NPs 2	0.45
L-ASNase/BSA-DOX Glu. NPs 3	0.50
Average L-ASNase/BSA-DOX Glu. NPs	0.34 ± 0.24
L-ASNase/BSA-DOX DTSSP NPs 1	0.34
L-ASNase/BSA-DOX DTSSP NPs 2	0.16
L-ASNase/BSA-DOX DTSSP NPs 3	0.20
Average L-ASNase/BSA-DOX DTSSP NPs	0.23 ± 0.09
Overall Average L-ASNase/DOX NPs	0.38 ± 0.12
Overall Average L-ASNase/BSA-DOX NPs	0.29 ± 0.09

3.9—Determination of L-ASNase Activity in NPs

A colorimetric assay was used to evaluate the impact of encapsulation on proteins' enzymatic activity. The asparaginase activity was determined by a coupled enzyme assay using a Sigma-Aldrich asparaginase activity assay kit. In the assay, asparaginase hydrolyzes L-asparagine to generate L-aspartate, which is converted to pyruvate and subsequently reacts with a colorless probe to form a stable chromophore that can be detected colorimetrically at 570 nm, which is proportional to the aspartate generated. The asparaginase activity is reported as nmole/min/mL or mU/mL, where one unit of asparaginase is defined as the amount of enzyme that generates 1.0 μmol of aspartate per minute at 25 °C. The amount of aspartate generated by encapsulated L-ASNase enzymes was determined using a calibration curve for aspartate standards, and the asparaginase activity was calculated using Equation 4 below.

$$Encapsulation\ Efficiency = \frac{B\ x\ Sample\ Dilution\ Factor}{(T_{final}\ -\ T_{initial})\ x\ V} \qquad Equation\ 4$$

B is the amount of aspartate (nmole) generated between $T_{initial}$ and T_{final}, where $T_{initial}$ is the time of first absorbance reading in minutes, and Tfinal is the time of second reading in minutes, and V is the sample volume (mL) added to a well.

Figure 32 illustrates a graphical representation of normalized activities of free L-ASNase, L-ASNase only NPs, L-ASNase/DOX, and L-ASNase/BSA-DOX NPs and Table 6 reports all the activities. The asparaginase activity of encapsulated L-ASNase has reduced by 25-30% compared to the positive control of free L-ASNase. A one-way ANOVA at a significance of 0.05 revealed that there was no statistically significant difference in mean activity between L-ASNase Only NPs, L-ASNase/DOX NPs, and L-ASNase/BSA-DOX NPs, p = 0.327. However, there was a statistically significant difference observed between all three types of NPs and free L-ASNase, p = 0.0001. A decrease in activity following encapsulation is expected and potentially caused by a few different factors, including steric hindrance, conformational changes caused by encapsulation, such as the formation of salt bridges, or diffusion-controlled access to the enzyme's active site within NPs.

Table 6. L-ASNase activity (nmol/min/mL) and normalized L-ASNase activity.

NPs Description	L-ASNase Activity (nmol/min/mL)	Normalized L-ASNase Activity
Free L-ASNase	9.4424 ± 0.4454	1.0000 ± 0.0667
L-ASNase Only NPs	6.7691 ± 0.3193	0.7169 ± 0.0478
L-ASNase/DOX Glu. NPs	7.2890 ± 0.3438	0.7719 ± 0.0515
L-ASNase/DOX DTSSP. NPs	5.8294 ± 0.2750	0.6174 ± 0.0412
L-ASNase/BSA-DOX Glu. NPs	7.5847 ± 0.3578	0.8033 ± 0.0536
L-ASNase/BSA-DOX DTSSP NPs	6.6454 ± 0.3134	0.7038 ± 0.0469
Average L-ASNase/DOX NPs	6.5592 ± 1.0321	0.6947 ± 0.1093
Average L-ASNase/BSA-DOX NPs	7.1151 ± 0.6642	0.7535 ± 0.07034

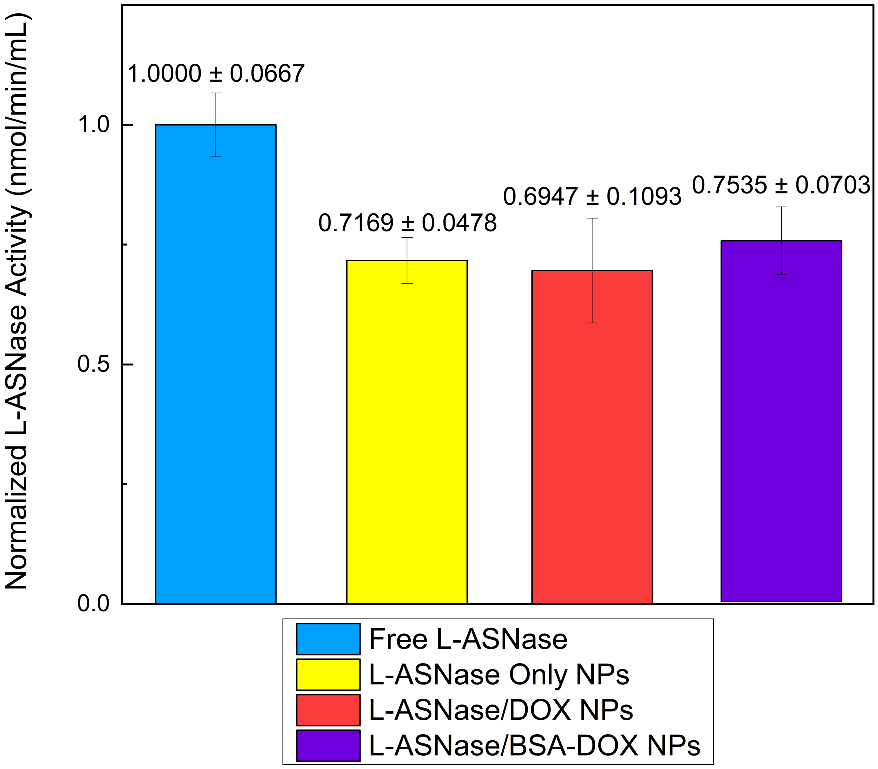

Figure 32 Normalized L-ASNase activity of L-ASNase/DOX NPs and L-ASNase/BSA-DOX NPs. Light blue, yellow, red, and purple represent free L-ASNase, L-ASNase Only NPs, L-ASNase/DOX NPs, and L-ASNase/BSA-DOX NPs, respectively. Free L-ASNase (positive control), normalized activity, 1.0000 ± 0.0667; L-ASNase Only NPs, normalized activity, 0.7169 ± 0.0478; L-ASNase/DOX NPs, 0.6947 ± 0.1093; L-ASNase/BSA-DOX NPs, normalized activity, 0.7535 ± 0.07034.

3.10—Quantification of DOX in Co-encapsulated NPs: A Preliminary Study

A calibration curve was used to determine the amount of DOX (mg) successfully encapsulated in NPs. The resulting amounts were subsequently used to determine the encapsulation efficiency using Equation 2 stated in the experimental chapter. A simple calibration curve was developed by using 6 DOX standards. DOX exhibits a strong maximum absorbance at 482 nm. The resulting calibration curve exhibited an R^2 value of 0.99966. NPs were washed using 100 kDa centrifugal concentrators at 11,337 rcf to eliminate un-encapsulated DOX from the samples. To ensure that conjugated DOX exhibited the same absorbance characteristics, BSA-L-ASNase/BSA-DOX NPs were incubated overnight with 10 mM of GSH to cleave the disulfide bonds and release DOX from the BSA-DOX conjugates within NPs. This method is yet to be optimized as there may be several factors affecting this experimental approach, such as the optimal incubation time to release all the DOX from BSA-DOX conjugates within NPs. For this preliminary study, the NPs were only incubated overnight in GSH, and below, we summarize our preliminary data from this experiment.

Figure 34 summarizes the average amount of DOX encapsulated (mg) and the encapsulation efficiency for L-ASNase/DOX NPs and L-ASNase/BSA-DOX NPs. The preliminary data show that the L-ASNase/DOX NPs co-encapsulated slightly more DOX at 0.013 ± 0.001 mg, while L-ASNase/BSA-DOX NPs co-encapsulated at 0.007 ± 0.001 mg. Despite the slight differences in co-encapsulation, L-ASNase/BSA-DOX NPs had better encapsulation efficiency at 22.72 ± 2.06%, while L-ASNase/DOX NPs showed an encapsulation efficiency of 13.12 ± 0.52%. The low encapsulation efficiency for DOX indicates that although free DOX may initially be encapsulated in larger amounts, it cannot retain DOX within the nanocarrier. Due to its very small molecular size, free DOX may be prematurely released from L-ASNaseDOX NPs through the polymer matrix.

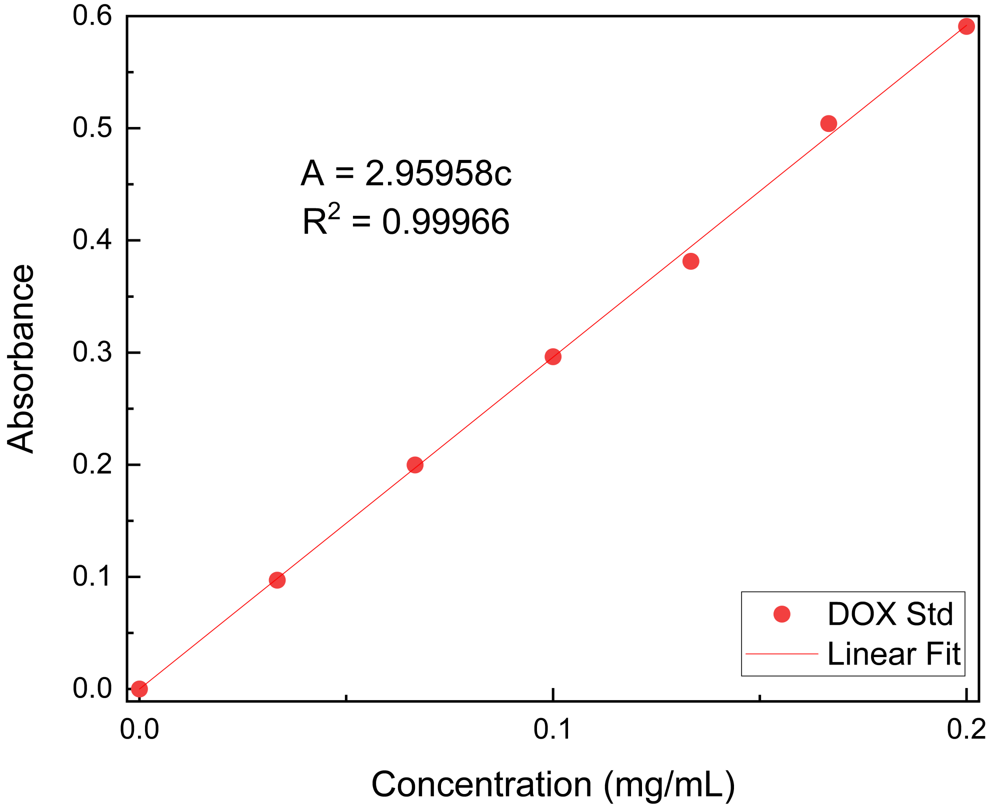

Figure 33 Calibration curve of DOX standards ranging from 0-0.2 mg/mL Slope, 2.95958 ± 0.0223 c; R^2, 0.99966.

Table 7. Determined DOX amount (mg) and encapsulation efficiency (%).

NPs Description Encapsulated DOX	Amount (mg)	Encapsulation Efficiency (%)
L-ASNase/DOX Glu. NPs 1	0.015 ± 0.004	14.83 ± 4.20
L-ASNase/DOX Glu. NPs 2	0.006 ± 0.004	6.16 ± 4.20
L-ASNase/DOX Glu. NPs 3	0.021 ± 0.015	20.85 ± 15.18
Average L-ASNase/DOX Glu. NPs	0.014 ± 0.004	13.94 ± 3.69
L-ASNase/DOX DTSSP NPs 1	0.029 ± 0.009	29.57 ± 9.00
L-ASNase/DOX DTSSP NPs 2	0.003 ± 0.002	3.51 ± 1.75
L-ASNase/DOX DTSSP NPs 3	0.004 ± 0.002	3.83 ± 2.16
Average L-ASNase/DOX DTSSP NPs	0.012 ± 0.007	12.30 ± 7.48
L-ASNase/BSA-DOX Glu. NPs 1	0.009 ± 0.003	30.14 ± 10.87
L-ASNase/BSA-DOX Glu. NPs 2	0.011 ± 0.004	34.63 ± 12.17
L-ASNase/BSA-DOX Glu. NPs 3	0.004 ± 0.002	13.17 ± 7.19
Average L-ASNase/BSA-DOX Glu. NPs	0.008 ± 0.002	25.98 ± 5.66
L-ASNase/BSA-DOX DTSSP NPs 1	0.003 ± 0.005	10.80 ± 14.80
L-ASNase/BSA-DOX DTSSP NPs 2	0.008 ± 0.002	26.15 ± 6.06
L-ASNase/BSA-DOX DTSSP NPs 3	0.007 ± 0.002	21.47 ± 5.95
Average L-ASNase/BSA-DOX DTSSP NPs	0.006 ± 0.001	19.47 ± 3.94
Overall Average L-ASNase/DOX NPs	0.013 ± 0.001	13.12 ± 0.52
Overall Average L-ASNase/BSA-DOX NPs	0.007 ± 0.001	22.72 ± 2.06

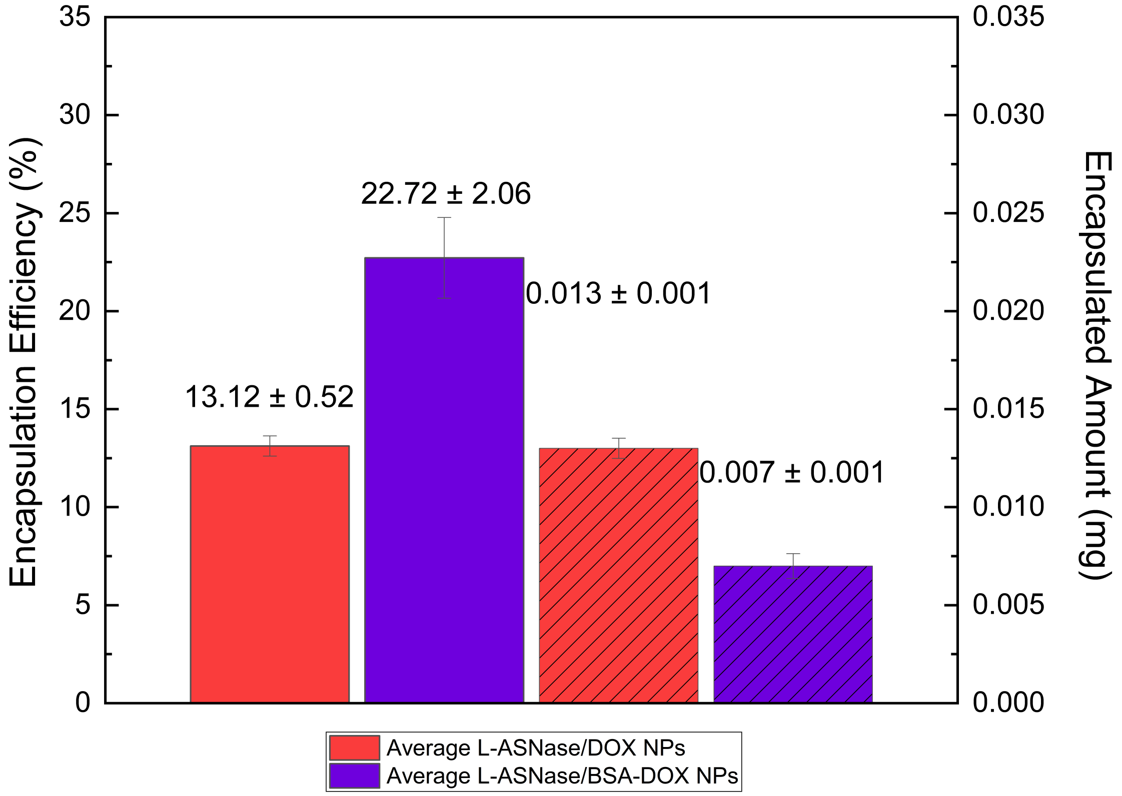

Figure 34 Encapsulated efficiency (%) and encapsulated DOX amount (mg). Red represents L-ASNase/DOX NPs, and purple represents L-ASNase/BSA-DOX NPs. The diagonal lines correspond to the second axis (encapsulated amount). L-ASNase/DOX NPs, encapsulation efficiency, 13.12 ± 0.52%, encapsulated amount, 0.013 ± 0.001 mg; L-ASNase/BSA-DOX NPs, encapsulation efficiency, 22.72 ± 2.06%, encapsulated amount, 0.007 ± 0.001 mg.

3.11—Qualitative Evaluation of DOX Encapsulation using HPLC

HPLC was utilized as a qualitative method to analyze the washed fractions of NPs for free DOX. As stated in the experimental section, L-ASNase/DOX NPs and L-ASNase NPs/BSA-DOX were washed three times using 100 kDa centrifugal concentrators at 11,337 rcf, and the washings were collected for HPLC analysis.

It is well established that DOX forms dimers in salt-containing solutions, such as buffers [47]. Two distinct peaks corresponding to DOX monomers and dimers were observed. Monomers eluted at approximately 11 minutes, and dimers eluted at later retention times around 19.5 minutes. The chromatograms containing washed fractions of L-ASNase/DOX NPs exhibited two peaks that align with those observed in the free DOX standard. This further indicates that free DOX is leaching out of the NPs. The chromatograms containing washed fractions of L-ASNase/BSA-DOX NPs showed peaks with lower intensities at the same retention times; although this is not a quantitative determination, this data suggests that the BSA-DOX conjugation effectively stabilizes DOX within nanocarriers, resulting in minimal levels of free DOX present in washed fractions.

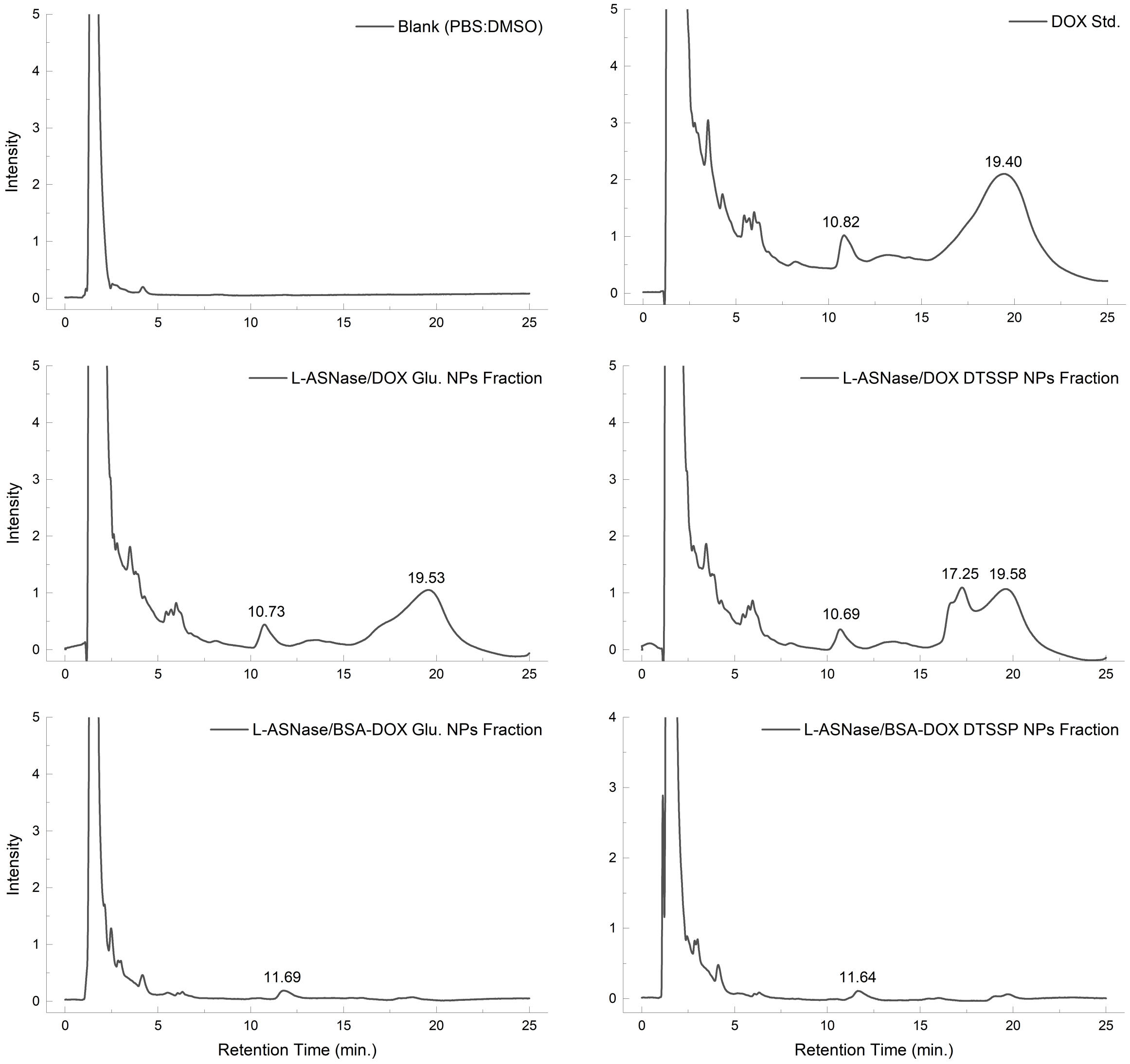

Figure 35 HPLC chromatograms of L-ASNase/DOX NPs and L-ASNase/BSA-DOX NPs washed fractions. Blank, no clear peaks observed past solvent peak; DOX std, monomer, 10.82 min., dimer, 19.40 min.; L-ASNase/DOX Glu. NPs, monomer, 10.73 min., dimer, 19.53 min.; L-ASNase/DOX DTSSP NPs, monomer, 10.69 min., dimer, 19.56 min.; L-ASNase/BSA-DOX Glu. NPs, monomer, 11.69; L-ASNase/BSA-DOX NPs, monomer, 11.64 min.

CHAPTER IV

CONCLUSION AND FUTURE DIRECTIONS

4.1—Conclusion

In this study, we successfully co-encapsulated DOX (DOX) and L-ASNase within PLL-g-PEG polymer nanocarriers. Initially, free L-ASNase/DOX NPs were formed via electrostatic interactions between the cationic polymer and negatively charged L-ASNase, resulting in self-assembled NPs. However, HPLC analysis revealed that L-ASNase/DOX NPs fail to retain the free DOX, releasing it into the surrounding solution. To enhance DOX stability within nanocarriers and improve synthesis outcomes, DOX was conjugated to the surface of BSA. UV-Vis spectroscopy confirmed the successful conjugation of DOX to BSA via lysine residues, and SDS-PAGE analysis verified that BSA's overall molecular weight remained unaltered post-conjugation. L-ASNase/DOX NPs exhibited significantly larger hydrodynamic diameters and high size variability, with an average size of approximately 415.3 ± 344.8 nm, indicating that this method was less effective in forming stable nanocarriers. Conversely, L-ASNase/BSA-DOX NPs demonstrated lower size variability and smaller hydrodynamic diameters, averaging around 84.8 ± 48.0 nm. In both NP types, L-ASNase encapsulation efficiencies ranged from 75% to 94%. As expected, L-ASNase activity decreased by 25–30%. Both types of NPs co-encapsulated DOX at similar levels. However, DOX can readily escape from the L-ASNase/DOX NPs, thereby reducing their encapsulation efficiency. In contrast, DOX encapsulation was stable within L-ASNase/BSA-DOX NPs, resulting in higher encapsulation efficiencies. In summary, we have successfully developed a method for co-encapsulating DOX and L-ASNase within PLL-g-PEG NPs.

4.2—Future Directions

The future avenues of research will focus on several key areas including (1) evaluation and optimization of drug release in the presence of various concentrations of GSH; (2) surface functionalization of L-ASNase/BSA-DOX NPs using cell-penetrating peptides for cellular targeting; (3) in vitro studies of surface-functionalized NPs with HEK293 to evaluate ability to cross cellular membranes; and (4) the co-encapsulation of other proteins and small molecule drugs through protein-drug conjugation. Optimizing drug release is crucial for achieving controlled therapeutic delivery and is essential for advancing NP-based cancer therapy. Linkers using disulfide bonds can be selectively cleaved in the high-GSH environment typical of cancer cells, thereby releasing the therapeutics. Surface functionalization enables the specific targeting of therapeutics to cancer cells. Peptides are designed to interact with surface cell receptors to target the NP cargo toward cancer tissues. Evaluation of the ability of functionalized NPs to cross cellular membranes will provide insight into cellular uptake and the potential for high drug delivery efficacy. Finally, other proteins and small molecule drugs may be suitable for co-encapsulation through this method. This method not only successfully co-encapsulated DOX and L-ASNase but can serve as a model for co-encapsulating other similar proteins and small molecule drugs. The application of this method to other therapies could unlock significant potential for novel treatment combinations.

REFERENCES

(1) Ferlay J., Ervik M., Lam F., Colombet M., Mery L., Piñeros M., et al. Global Cancer Observatory: Cancer Today. Lyon: International Agency for Research on Cancer; **2020**

(2) Karar, M. E.; Alotaibi, B.; Alotaibi, M. Intelligent Medical IOT-Enabled Automated Microscopic Image Diagnosis of Acute Blood Cancers. *Sensors* **2022**, *22* (6), 2348. DOI:10.3390/s22062348.

(3) Copelan, E. A.; McGuire, E. A. The Biology and Treatment of Acute Lymphoblastic Leukemia in Adults. *Blood* **1995**, *85* (5), 1151–1168. DOI:10.1182/blood.v85.5.1151.bloodjournal855115.

(4) Talati, C. Difference between Acute and Chronic Leukemia. https://www.moffitt.org/cancers/leukemia/faqs/what-is-the-difference-between-acute-and-chronic-leukemia/ (accessed 2025-02-15).

(5) Campos-Sanchez, E.; Toboso-Navasa, A.; Romero-Camarero, I.; Barajas-Diego, M.; Sánchez-García, I.; Cobaleda, C. Acute Lymphoblastic Leukemia and Developmental Biology. *Cell Cycle* **2011**, *10* (20), 3473–3486. DOI:10.4161/cc.10.20.17779.

(6) Abed, H. F.; Abuwatfa, W. H.; Husseini, G. A. Redox-Responsive Drug Delivery Systems: A Chemical Perspective. *Nanomaterials* **2022**, *12* (18), 3183. DOI:10.3390/nano12183183.

(7) Ruttala, H. B.; Ramasamy, T.; Madeshwaran, T.; Hiep, T. T.; Kandasamy, U.; Oh, K. T.; Choi, H.-G.; Yong, C. S.; Kim, J. O. Emerging Potential of Stimulus-Responsive Nanosized Anticancer Drug Delivery Systems for Systemic Applications. *Archives of Pharmacal Research* **2017**, *41* (2), 111–129. DOI:10.1007/s12272-017-0995-x.

(8) Bahreini, E.; Aghaiypour, K.; Abbasalipourkabir, R.; Mokarram, A. R.; Goodarzi, M. T.; Saidijam, M. Preparation and Nanoencapsulation of L-Asparaginase II in Chitosan-Tripolyphosphate Nanoparticles and in Vitro Release Study. *Nanoscale Research Letters* **2014**, *9* (1), 340. DOI:10.1186/1556-276x-9-340.

(9) Wang, N.; Ji, W.; Wang, L.; Wu, W.; Zhang, W.; Wu, Q.; Du, W.; Bai, H.; Peng, B.; Ma, B.; Li, L. Overview of the Structure, Side Effects, and Activity Assays of l-Asparaginase as a Therapy Drug of Acute Lymphoblastic Leukemia. *RSC Medicinal Chemistry* **2022**, *13* (2), 117–128. DOI:10.1039/d1md00344e.

(10) Kumar, K.; Kaur, J.; Walia, S.; Pathak, T.; Aggarwal, D. L-Asparaginase: An Effective Agent in the Treatment of Acute Lymphoblastic Leukemia. *Leukemia & Lymphoma* **2013**, *55* (2), 256–262. DOI:10.3109/10428194.2013.803224.

(11) Richards, N. G.; Kilberg, M. S. Asparagine Synthetase Chemotherapy. *Annual Review of Biochemistry* **2006**, *75* (1), 629–654. DOI:10.1146/annurev.biochem.75.103004.142520.

(12) Van Trimpont, M.; Peeters, E.; De Visser, Y.; Schalk, A. M.; Mondelaers, V.; De Moerloose, B.; Lavie, A.; Lammens, T.; Goossens, S.; Van Vlierberghe, P. Novel Insights on the Use of L-Asparaginase as an Efficient and Safe Anti-Cancer Therapy. *Cancers* **2022**, *14* (4), 902. DOI:10.3390/cancers14040902.

(13) Avramis VI. Asparaginases: biochemical pharmacology and modes of drug resistance. *Anticancer Res.* **2012**, *32* (7), 2423-37. PMID: 22753699.

(14) Ueno, T.; Ohtawa, K.; Mitsui, K.; Kodera, Y.; Hiroto, M.; Matsushima, A.; Inada, Y.; Nishimura, H. Cell Cycle Arrest and Apoptosis of Leukemia Cells Induced by L-Asparaginase. *Leukemia* **1997**, *11* (11), 1858–1861. DOI:10.1038/sj.leu.2400834.

(15) De Morais, S.; De Souza, T. Human L-asparaginase: Acquiring Knowledge of Its Activation (Review). *International Journal of Oncology* **2021**, *58* (4), 11. DOI:10.3892/ijo.2021.5191.

(16) Harish, V.; Tewari, D.; Gaur, M.; Yadav, A. B.; Swaroop, S.; Bechelany, M.; Barhoum, A. Review on Nanoparticles and Nanostructured Materials: Bioimaging, Biosensing, Drug Delivery, Tissue Engineering, Antimicrobial, and Agro-Food Applications. *Nanomaterials* **2022**, *12* (3), 457. DOI:10.3390/nano12030457.

(17) Kaialy, W.; Al Shafiee, M. Recent Advances in the Engineering of Nanosized Active Pharmaceutical Ingredients: Promises and Challenges. *Advances in Colloid and Interface Science* **2016**, 228, 71–91. DOI:10.1016/j.cis.2015.11.010.

(18) Buzea, C.; Pacheco, I. I.; Robbie, K. Nanomaterials and Nanoparticles: Sources and Toxicity. *Biointerphases* **2007**, *2* (4), 17–71. DOI:10.1116/1.2815690.

(19) Smijs, T.; Pavel, S. Titanium Dioxide and Zinc Oxide Nanoparticles in Sunscreens: Focus on Their Safety and Effectiveness. Nanotechnology, ***Science and Applications*** **2011**, 4, 95–112. DOI:10.2147/nsa.s19419.

(20) Sim, S.; Wong, N. Nanotechnology and Its Use in Imaging and Drug Delivery (Review). *Biomedical Reports* **2021**, *14* (5), 42. DOI:10.3892/br.2021.1418.

(21) Zielińska, A.; Carreiró, F.; Oliveira, A. M.; Neves, A.; Pires, B.; Venkatesh, D. N.; Durazzo, A.; Lucarini, M.; Eder, P.; Silva, A. M.; Santini, A.; Souto, E. B. Polymeric Nanoparticles: Production, Characterization, *Toxicology and Ecotoxicology. Molecules* **2020**, *25* (16), 3731. DOI:10.3390/molecules25163731.

(22) Altammar, K. A. A Review on Nanoparticles: Characteristics, Synthesis, Applications, and Challenges. *Frontiers in Microbiology* **2023**, 14. DOI:10.3389/fmicb.2023.1155622.

(23) Chenthamara, D.; Subramaniam, S.; Ramakrishnan, S. G.; Krishnaswamy, S.; Essa, M. M.; Lin, F.-H.; Qoronfleh, M. W. Therapeutic Efficacy of Nanoparticles and Routes of Administration. *Biomaterials Research* **2019**, *23* (1). DOI:10.1186/s40824-019-0166-x.

(24) Sahoo, S.; Gopalan, A.; Ramesh, S.; Nirmala, P.; Ramkumar, G.; Agnes Shifani, S.; Subbiah, R.; Isaac JoshuaRamesh Lalvani, J. Preparation of Polymeric Nanomaterials Using Emulsion Polymerization. *Advances in Materials Science and Engineering* **2021**, (1). DOI:10.1155/2021/1539230.

(25) Choi, Y. H.; Liu, F.; Kim, J.-S.; Choi, Y. K.; Sang Park a, J.; Kim, S. W. Polyethylene Glycol-Grafted Poly-L-Lysine as Polymeric Gene Carrier. *Journal of Controlled Release* **1998**, *54* (1), 39–48. DOI:10.1016/s0168-3659(97)00174-0.

(26) Krieger, A.; Zika, A.; Gröhn, F. Functional Nano-Objects by Electrostatic Self-Assembly: Structure, Switching, and Photocatalysis. *Frontiers in Chemistry* **2022**, 9, 779360. DOI:10.3389/fchem.2021.779360.

(27) Perumal, S. Polymer Nanoparticles: Synthesis and Applications. *Polymers* **2022**, *14* (24), 5449. DOI:10.3390/polym14245449.

(28) Kahraman, E.; Güngör, S.; Özsoy, Y. Potential Enhancement and Targeting Strategies of Polymeric and Lipid-Based Nanocarriers in Dermal Drug Delivery. Therapeutic Delivery 2017, *8* (11), 967–985. DOI:10.4155/tde-2017-0075.

(29) Peng Zhang, Fang Sun, Caroline Tsao, Sijun Liu, Priyesh Jain, Andrew Sinclair, Hsiang-Chieh Hung, Tao Bai, Kan Wu, and Shaoyi Jiang; Zwitterionic gel encapsulation promotes protein stability, enhances pharmacokinetics, and reduces immunogenicity, PNAS 2015, *112* (39), 12046-12051.

(30) Chakrabarty, A. M.; Bernardes, N.; Fialho, A. M. Bacterial Proteins and Peptides in Cancer Therapy. *Bioengineered* **2014**, *5* (4), 234–242. DOI:10.4161/bioe.29266.

(31) Sanches, M.; Barbosa, J. A.; de Oliveira, R. T.; Abrahão Neto, J.; Polikarpov, I. Structural Comparison ofEscherichia Colil-Asparaginase in Two Monoclinic Space Groups. *Acta Crystallographica Section D Biological Crystallography* **2003**, *59* (3), 416–422. DOI:10.1107/s0907444902021200.

(32) Lang S, Uber desamidierung im Tierkorper Beitr. *Chem. Physiol. Pathol*. **1904**, 5 321–45

(33) Ulu, A.; Ates, B. Immobilization Ofl-Asparaginase on Carrier Materials: A Comprehensive Review. *Bioconjugate Chemistry* **2017**, *28* (6), 1598–1610. DOI:10.1021/acs.bioconjchem.7b00217.

(34) Swain, A. L.; Jaskólski, M.; Housset, D.; Rao, J. K.; Wlodawer, A. Crystal Structure of Escherichia Coli L-Asparaginase, an Enzyme Used in Cancer Therapy. *Proceedings of the National Academy of Sciences* **1993**, *90* (4), 1474–1478. DOI:10.1073/pnas.90.4.1474.

(35) Kozak, M.; Jurga, S. A Comparison between the Crystal and Solution Structures of Escherichia Coli Asparaginase II. *Acta Biochimica Polonica* **2002**, *49* (2), 509–513. DOI:10.18388/abp.2002_3810.

(36) Narta, U. K.; Kanwar, S. S.; Azmi, W. Pharmacological and Clinical Evaluation of L-Asparaginase in the Treatment of Leukemia. *Critical Reviews in Oncology/Hematology* **2007**, *61* (3), 208–221. DOI:10.1016/j.critrevonc.2006.07.009.

(37) Avramis, V. I.; Tiwari, P. N. Effect of Lisinopril Treatment on Genotoxicity of L-Asparaginase (Asnase) in Bone Marrow Stem Cells for Aculte Lymphoblstic Leukemia (ALL). *International Journal of Clinical and Medical Education Research* **2022**, *1* (5), 241–254. DOI:10.33140/ijcmer.01.05.01.

(38) Egler, R. A.; Ahuja, S. P.; Matloub, Y. L-Asparaginase in the Treatment of Patients with Acute Lymphoblastic Leukemia. *Journal of Pharmacology and Pharmacotherapeutics* **2016**, *7* (2), 62–71. DOI:10.4103/0976-500x.184769.

(39) Hermanova, I.; Arruabarrena-Aristorena, A.; Valis, K.; Nuskova, H.; Alberich-Jorda, M.; Fiser, K.; Fernandez-Ruiz, S.; Kavan, D.; Pecinova, A.; Niso-Santano, M.; Zaliova, M.; Novak, P.; Houstek, J.; Mracek, T.; Kroemer, G.; Carracedo, A.; Trka, J.; Starkova, J. Pharmacological Inhibition of Fatty-Acid Oxidation Synergistically Enhances the Effect of L-Asparaginase in Childhood All Cells. *Leukemia* **2015**, *30* (1), 209–218. DOI:10.1038/leu.2015.213.

(40) Song, P.; Ye, L.; Fan, J.; Li, Y.; Zeng, X.; Wang, Z.; Wang, S.; Zhang, G.; Yang, P.; Cao, Z.; Ju, D. Asparaginase Induces Apoptosis and Cytoprotective Autophagy in Chronic Myeloid Leukemia Cells. *Oncotarget* **2015**, *6* (6), 3861–3873. DOI:10.18632/oncotarget.2869.

(41) Liu, B.; Zhou, H.; Tan, L.; Siu, K. T.; Guan, X.-Y. Exploring Treatment Options in Cancer: Tumor Treatment Strategies. *Signal Transduction and Targeted Therapy* **2024**, *9* (1). DOI:10.1038/s41392-024-01856-7.

(42) Chattopadhyay, S.; Hazra, R.; Mallick, A.; Gayen, S.; Roy, S. Small-Molecule in Cancer Immunotherapy: Revolutionizing Cancer Treatment with Transformative, Game-Changing Breakthroughs. *Biochimica et Biophysica Acta (BBA) - Reviews on Cancer* **2024**, *1879* (5), 189170. DOI:10.1016/j.bbcan.2024.189170.

(43) Iqbal, N.; Iqbal, N. Imatinib: A Breakthrough of Targeted Therapy in Cancer. *Chemotherapy Research and Practice* **2014,** *2020* (1), 1–9. DOI:10.1155/2014/357027.

(44) Nitiss, J. L. DNA Topoisomerase II and Its Growing Repertoire of Biological Functions. *Nature Reviews Cancer* **2009**, *9* (5), 327–337. DOI:10.1038/nrc2608.

(45) Yakkala, P. A.; Penumallu, N. R.; Shafi, S.; Kamal, A. Prospects of Topoisomerase Inhibitors as Promising Anti-Cancer Agents. *Pharmaceuticals* **2023**, *16* (10), 1456. DOI:10.3390/ph16101456.

(46) Srinivasan, M.; Rajabi, M.; A. Mousa, S. Nanobiomaterials in Cancer Therapy. *Nanobiomaterials in Cancer Therapy* **2016**, 7, 57–89. DOI:10.1016/b978-0-323-42863-7.00003-7.

(47) Yamada, Y. Dimerization of Doxorubicin Causes Its Precipitation. *ACS Omega* **2020**, *5* (51), 33235–33241. DOI:10.1021/acsomega.0c04925.

(48) Santra, S.; Kaittanis, C.; Grimm, J.; Perez, J. M. Drug/Dye-loaded, Multifunctional Iron Oxide Nanoparticles for Combined Targeted Cancer Therapy and Dual Optical/Magnetic Resonance Imaging. *Small* **2009**, *5* (16), 1862–1868. DOI:10.1002/smll.200900389.

(49) Fumoto, S.; Nishida, K. Co-Delivery Systems of Multiple Drugs Using Nanotechnology for Future Cancer Therapy. *Chemical and Pharmaceutical Bulletin* **2020**, *68* (7), 603–612. DOI:10.1248/cpb.c20-00008.

(50) Bhattacharjee, S. Craft of Co-Encapsulation in Nanomedicine: A Struggle to Achieve Synergy through Reciprocity. *ACS Pharmacology Translational Science* **2022**, *5* (5), 278–298. DOI:10.1021/acsptsci.2c00033.

(51) Hikkaduwa Koralege, R. S.; Sahoo, K.; Flynn, N.; Liu, J.; Ranjan, A.; Pope, C.; Ramsey, J. D. Erythrocytes Internalize Nanoparticles Functionalized with Low Molecular Weight Protamine. *Journal of NanoparticleResearch* **2021**, *23* (4). DOI:10.1007/s11051-021-05202-8.

(52) Goff, K.; Dean, D.; Helms, I.; Hatton, R.; Hines, R.; Hikkaduwa Koralege, R. S. Evaluation of Long-Term Stability of L-Asparaginase Encapsulated PLL-g-Peg Nanoparticles in Solution to Aid in Therapeutic Delivery. *Nano Express* **2024**, *5* (4), 045001. DOI:10.1088/2632-959x/ad80b3.

(53) Sawhney, A. S.; Hubbell, J. A. Poly(Ethylene Oxide)-Graft-Poly(L-Lysine) Copolymers to Enhance the Biocompatibility of Poly(l-Lysine)-Alginate Microcapsule Membranes. *Biomaterials* **1992**, *13* (12), 863–870. DOI:10.1016/0142-9612(92)90180-v.

(54) Biagiotti, S.; Paoletti, M. F.; Fraternale, A.; Rossi, L.; Magnani, M. Drug Delivery by Red Blood Cells. *IUBMB Life* **2011**, *63* (8), 621–631. DOI:10.1002/iub.478.

(55) Koleva, L.; Bovt, E.; Ataullakhanov, F.; Sinauridze, E. Erythrocytes as Carriers: From Drug Delivery to Biosensors. *Pharmaceutics* **2020**, *12* (3), 276. DOI:10.3390/pharmaceutics12030276.

(56) Salem, M., Mauguen, Y., & Prangé, T. Revisiting glutaraldehyde cross-linking: The case of the Arg-Lys intermolecular doublet. Acta Crystallographica Section F: *Structural Biology and Crystallization Communications* **2010**, *66* (3), 225–228. DOI:10.1107/S1744309109054037.

(57) Lambert, W.; Söderberg, C. A.; Rutsdottir, G.; Boelens, W. C.; Emanuelsson, C. Thiol-exchange in DTSSP Crosslinked Peptides Is Proportional to Cysteine Content and Precisely Controlled in Crosslink Detection by Two-step LC-MALDI MSMS. *Protein Science* **2011**, *20* (10), 1682–1691. DOI:10.1002/pro.699.

(58) Fologea, D., Ledden, B., McNabb, D. S., & Li, J. Electrical characterization of protein molecules by a solid-state nanopore. *Applied Physics Letters* **2007**, *91* (5), 539011–539013. DOI:10.1063/1.2767206

(59) Abbas, I.; Schwaar, T.; Bienwald, F.; Weller, M. Predictable Peptide Conjugation Ratios by Activation of Proteins with Succinimidyl Iodoacetate (SIA). *Methods and Protocols* **2017**, *1* (1), 2. DOI:10.3390/mps1010002.

(60) Hu, M.; Liu, H.; Zhang, Y.; Lu, D.; Zheng, L.; Wang, Y.; Chen, S.; Liu, T. Preparation and Evaluation of the Pd0721-dox Antibody-drug Conjugate Targeting EGFRVIII to Inhibit Glioblastoma. *Experimental and Therapeutic Medicine* **2024**, *27* (6), 254. DOI:10.3892/etm.2024.12542.

(61) Santra, S.; Kaittanis, C.; Santiesteban, O. J.; Perez, J. M. Cell-Specific, Activatable, and Theranostic Prodrug for Dual-Targeted Cancer Imaging and Therapy. *Journal of the American Chemical Society* **2011**,*133* (41), 16680–16688. DOI:10.1021/ja207463b.

(62) Flynn, N.; Topal, Ö.; Hikkaduwa Koralege, R. S.; Hartson, S.; Ranjan, A.; Liu, J.; Pope, C.; Ramsey, J. D. Effect of Cationic Grafted Copolymer Structure on the Encapsulation of Bovine Serum Albumin. *Materials Science and Engineering: C* **2016**, *62*, 524–531. DOI:10.1016/j.msec.2016.01.092.

(63) Pasek-Allen, J. L.; Wilharm, R. K.; Bischof, J. C.; Pierre, V. C. NMR Characterization of Polyethylene Glycol Conjugates for Nanoparticle Functionalization. *ACS omega*, **2023,** *8* (4), 4331–4336. DOI:10.1021/acsomega.2c07669.

(64) Tosatti, S.; Paul, S. M. D.; Askendal, A.; VandeVondele, S.; Hubbell, J. A.; Tengvall, P.; Textor, M. Peptide Functionalized Poly(l-Lysine)-g-Poly(Ethylene Glycol) on Titanium: Resistance to Protein Adsorption in Full Heparinized Human Blood Plasma. *Biomaterials* **2003**, *24* (27), 4949–4958. DOI:10.1016/s0142-9612(03)00420-4.

(65) Alexander, S.; Gomez, V.; Barron, A. R. Carboxylation and Decarboxylation of Aluminum Oxide Nanoparticles Using Bifunctional Carboxylic Acids and Octylamine. *Journal of Nanomaterials* **2016**, *2016*, 1–8. DOI:10.1155/2016/7950876.

(66) Varga, Z.; Mihály, J.; Berényi, Sz.; Bóta, A. Structural Characterization of the Poly(Ethylene Glycol) Layer of Sterically Stabilized Liposomes by Means of FTIR Spectroscopy. *European Polymer Journal* **2013**, *49* (9), 2415–2421. DOI:10.1016/j.eurpolymj.2013.02.025.

(67) Threlfall, T. The Infrared Spectra of Amides. Part 1. the Stretching Vibrations of Primary Carboxamides. *Vibrational Spectroscopy* **2022**, 121, 103386. DOI:10.1016/j.vibspec.2022.103386.

(68) Hu, M.; Liu, H.; Zhang, Y.; Lu, D.; Zheng, L.; Wang, Y.; Chen, S.; Liu, T. Preparation and Evaluation of the Pd0721-dox Antibody-drug Conjugate Targeting EGFRVIII to Inhibit Glioblastoma. *Experimental and Therapeutic Medicine* **2024**, *27* (6), 254. DOI:10.3892/etm.2024.12542.

(69) Zhang, R.; Zhu, J.; Sun, D.; Li, J.; Yao, L.; Meng, S.; Li, Y.; Dang, Y.; Wang, K. The Mechanism of Dynamic Interaction between Doxorubicin and Calf Thymus DNA at the Single-Molecule Level Based on Confocal Raman Spectroscopy. *Micromachines* **2022**, *13* (6), 940. DOI:10.3390/mi13060940.

(70) Awan, U. A.; Raza, A.; Ali, S.; Saeed, R. F.; Akhtar, N. Doxorubicin-Loaded Gold Nanorods: A Multifunctional Chemo-Photothermal Nanoplatform for Cancer Management. *Beilstein Journal of Nanotechnology* **2021**, *12*, 295–303. DOI:10.3762/bjnano.12.24.

(71) Ghosh, D.; Mondal, S.; Ghosh, S.; Saha, A. Protein Conformation Driven Biomimetic Synthesis of Semiconductor Nanoparticles. *J. Mater. Chem.* **2012**, *22* (2), 699–706. DOI:10.1039/c1jm13730a.

(72) Stevenson, H.; Bacon, A.; Joseph, K. M.; Gwandaru, W. R.; Bhide, A.; Sankhala, D.; Dhamu, V. N.; Prasad, S. A Rapid Response Electrochemical Biosensor for Detecting THC in Saliva. *Scientific Reports* **2019**, *9* (1), 12701. DOI:10.1038/s41598-019-49185-y.

(73) Li, X.; Gao, C.; Wu, Y.; Cheng, C.-Y.; Xia, W.; Zhang, Z. Combination Delivery of Adjudin and Doxorubicin via Integrating Drug Conjugation and Nanocarrier Approaches for the Treatment of Drug-Resistant Cancer Cells. *Journal of Materials Chemistry B* **2015**, *3* (8), 1556–1564. DOI:10.1039/c4tb01764a.

(74) Nguyen, T. X.; Chen, S.-S.; Chang, H.-M.; Cao, N. D.; Singh, R. Effects of Polyethylene Glycol and Glutaraldehyde Cross-Linker on TFC-Fo Membrane Performance. *Environmental Technology & Innovation* **2020**, *20*, 101059. DOI:10.1016/j.eti.2020.101059.

(75) Okuda, K.; Urabe, I.; Yamada, Y.; Okada, H. Reaction of Glutaraldehyde with Amino and Thiol Compounds. *Journal of Fermentation and Bioengineering* **1991**, *71* (2), 100–105. DOI:10.1016/0922-338x(91)90231-5.

(76) Maguire, C. M.; Rösslein, M.; Wick, P.; Prina-Mello, A. Characterisation of particles in solution - a perspective on light scattering and comparative technologies. *Sci Technol Adv Mater* **2018**, *19* (1), 732-745. DOI: 10.1080/14686996.2018.1517587.

(77) Krstić, M.; Medarević, Đ.; Đuriš, J.; Ibrić, S. Self-Nanoemulsifying Drug Delivery Systems (SNEDDS) and Self-Microemulsifying Drug Delivery Systems (SMEDDS) as Lipid Nanocarriers for Improving Dissolution Rate and Bioavailability of Poorly Soluble Drugs. *Chapter 12 - Lipid Nanocarriers for Drug Targeting* **2018**, 473–508. DOI:10.1016/b978-0-12-813687-4.00012-8.

(78) Gimsa, J.; Eppmann, P.; Prüger, B. Introducing Phase Analysis Light Scattering for Dielectric Characterization: Measurement of Traveling-Wave Pumping. *Biophysical Journal* **1997**, *73* (6), 3309–3316. DOI:10.1016/s0006-3495(97)78355-3.

(79) Metilli, L.; Francis, M.; Povey, M.; Lazidis, A.; Marty-Terrade, S.; Ray, J.; Simone, E. Latest Advances in Imaging Techniques for Characterizing Soft, Multiphasic Food Materials. *Advances in Colloid and Interface Science* **2020**, *279*, 102154. DOI:10.1016/j.cis.2020.102154.

(80) Nowakowski, A. B.; Wobig, W. J.; Petering, D. H. Native SDS-PAGE: High Resolution Electrophoretic Separation of Proteins with Retention of Native Properties Including Bound Metal Ions. *Metallomics* **2014**, *6* (5), 1068–1078. DOI:10.1039/c4mt00033a.

(81) El-Naggar, N. E.-A.; Deraz, S. F.; Soliman, H. M.; El-Deeb, N. M.; El-Ewasy, S. M. Purification, characterization, cytotoxicity and anticancer activities of L-asparaginase, anti-colon cancer protein, from the newly isolated alkaliphilic Streptomyces fradiae NEAE-82. *Scientific Reports* **2016**, *6* (1), 32926. DOI: 10.1038/srep32926.

(82) Lubkowski, J.; Wlodawer, A. Structural and biochemical properties of L-asparaginase. *Febs j* **2021**, *288* (14), 4183-4209. DOI: 10.1111/febs.16042.

(83) Yun, M. K.; Nourse, A.; White, S. W.; Rock, C. O.; Heath, R. J. Crystal structure and allosteric regulation of the cytoplasmic Escherichia coli L-asparaginase I. *J Mol Biol* **2007**, *369* (3), 794-811. DOI: 10.1016/j.jmb.2007.03.061.

(84) Liu, R.; Yue, Z.; Tsai, C.-C.; Shen, J. Assessing Lysine and Cysteine Reactivities for Designing Targeted Covalent Kinase Inhibitors. *Journal of the American Chemical Society* **2019**, *141* (16), 6553–6560. DOI:10.1021/jacs.8b13248.